

From Hope to Safety: Unlearning Biases of Deep Models via Gradient Penalization in Latent Space

Maximilian Dreyer^{1,*}, Frederik Pahde^{1,*}, Christopher J. Anders^{2,3}, Wojciech Samek^{1,2,3,†}, Sebastian Lapuschkin^{1,†}

¹Fraunhofer Heinrich Hertz Institut, Berlin, Germany

² Technische Universität Berlin, Berlin, Germany

³Berlin Institute for the Foundations of Learning and Data (BIFOLD), Berlin, Germany

[†]corresponding authors: {wojciech.samek, sebastian.lapuschkin}@hhi.fraunhofer.de

* contributed equally

Abstract

Deep Neural Networks are prone to learning spurious correlations embedded in the training data, leading to potentially biased predictions. This poses risks when deploying these models for high-stake decision-making, such as in medical applications. Current methods for post-hoc model correction either require input-level annotations which are only possible for spatially localized biases, or augment the latent feature space, thereby *hoping* to enforce the right reasons. We present a novel method for model correction on the concept level that *explicitly* reduces model sensitivity towards biases via gradient penalization. When modeling biases via Concept Activation Vectors, we highlight the importance of choosing robust directions, as traditional regression-based approaches such as Support Vector Machines tend to result in diverging directions. We effectively mitigate biases in controlled and real-world settings on the ISIC, Bone Age, ImageNet and CelebA datasets using VGG, ResNet and EfficientNet architectures. Code is available on <https://github.com/frederikpahde/frclarc>.

1 Introduction

For over a decade, Deep Neural Networks (DNNs) face a growing interest in industry and research, featuring application in fields such as medicine or autonomous driving due to their strong predictive performance. However, their high performance may potentially be inflated by *spurious correlations* in the training data, which can pose serious risks in safety-critical applications [12]. Several so called “short-cuts” have been found in medical settings, including hospital tags in COVID-19 radiographs [10], or skin markings for skin lesion detection [6]. Such short-cuts might also compromise fairness, as shown in Figure 1, where a DNN learned to use apparel features, *i.e.*, a collar, to infer that the hair is not blonde, due to overly-present dark-haired men wearing a suit in the training dataset. In the shown explanation heatmaps, red and blue color represent relevance for or against the prediction, respectively.

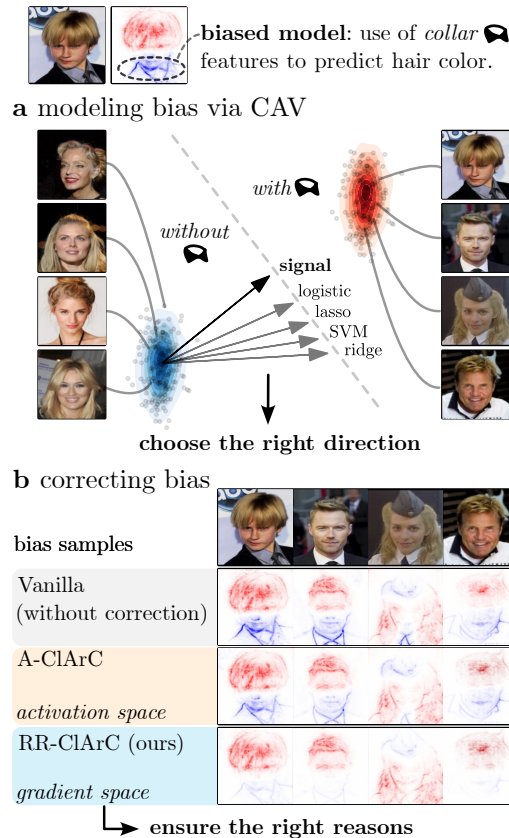


Figure 1: Our DNN bias correction method RR-CIArC consists of two steps: first finding the bias direction in the model’s latent space, and secondly reducing model sensitivity towards the direction in a fine-tuning step. **a)** When modeling the bias (here “collar”) via CAVs, robust approaches such as signal-CAV are key to model correction. Most traditional regression solvers (*e.g.*, SVMs) lead to diverging directions. **b)** Compared to activation-based methods, such as A-CIArC, that *implicitly* regularize model behavior, RR-CIArC *explicitly* reduces bias sensitivity via gradient penalization, ultimately reducing the relevance of the bias most strongly, as shown in the explanation heatmaps.

In order to reveal such spurious behavior, the field of eXplainable Artificial Intelligence (XAI) has proposed several techniques identifying irregularities in a model’s global behavior [19, 5, 24], or by studying individual predictions [34]. Acting on such findings, a variety of works perform post-hoc model correction by penalizing model attention on spurious features using pixel-wise input-level annotations [30, 28]. Whereas such annotations are highly labor-intensive and only applicable for spatially localized biases, *i.e.*, biases that can clearly be located in input space, the Class Artifact Compensation (CIArC)-framework proposes bias unlearning in a model’s latent feature space, requiring only sparse (sample-wise) annotations in the form of artifact labels [2]. The approach follows a common methodology in the field of latent concept interpretability: Biases are modeled using latent vectors, referred to as Concept Activation Vector (CAV) [17], which, importantly, can also describe spatially unlocalized biases, such as, *e.g.*, color shifts or static artifacts from imaging equipment, that (possibly) overlay sensible input features.

We find, however, that the effectiveness of the CIArC-framework’s model correction is limited by targeting only latent *activations*, which has two major drawbacks: (1) Manipulation of latent activations cannot be applied in a class-specific manner, and (2) biases may be only partially unlearned due to the method’s indirect regularization.

To *enforce* the use of the right reasons on the concept level, we present Right Reason CIArC (CIArC), an extension to CIArC which explicitly penalizes the model’s latent gradient along the bias direction. Thus, our method enables class-specific unlearning of localized, as well as unlocalized biases while only requiring sparse sample-wise label annotation for the computation of bias CAVs. Furthermore, these annotations can be acquired semi-automatically using available XAI tools, as illustrated in [24].

As suggested by [17], and followed in the CIArC framework, CAVs are usually computed using regression-based approaches such as Support Vector Machines (SVMs). However, we observe that common regression-based approaches hinder precise model correction caused by a tendency to diverge from the true concept direction due to, *e.g.*, noise in the data [14]. Only for the correlation-based signal-CAV [25] we observe a strong correlation of the modeled direction and the true concept direction.

Our contributions include the following:

1. We compare different CAV computation methods and observe significant shortcomings in widely used approaches such as SVMs, which deviate strongly from the true concept direction in controlled settings.
2. We present RR-CIArC, a novel method to correct model behavior using CAVs, which is based on the

latent gradient w.r.t. the model output, allowing for a class-specific unlearning of localized and unlocalized biases.

3. We evaluate the performance of RR-CIArC against other state-of-the-art methods in controlled settings on the ISIC, Bone Age and ImageNet datasets, as well as for a dataset-intrinsic bias in the CelebA dataset, using the VGG, ResNet and EfficientNet architectures.

2 Related Work

Earlier works describe the tendency of DNNs to discover shortcuts in training data [12], harming their generalization capabilities in real-world scenarios. Among other techniques [29, 23], XAI-based methods have proven as useful tools for the detection and removal of shortcuts learned by DNNs [19, 24, 37].

Most approaches for post-hoc model correction are based on input-level guidance. These either require spatial annotations of the bias in the form of segmentation masks, which are expensive to retrieve and only applicable for localized biases [28], or require a data augmentation of the bias to change the data distribution [31, 21]. The former group of methods aims at aligning a model’s attention with a pre-defined input-level prior by penalizing the use of undesired features. The popular method of Right for the Right Reason (RRR) [30], *e.g.*, achieves model correction hereby through regularization of the input gradient, introducing an additional loss term during fine-tuning.

Other recent works propose model correction on the concept-level, allowing to address biases that are not clearly localized in input space. While some are only applicable for interpretable architectures [4, 38], the CIArC-framework leverages CAVs to model the direction of undesired data artifacts in latent activation space [2]. CIArC-methods, however, are based on latent feature augmentation and thus do not support class-specific corrections. Our approach extends the CIArC framework by *explicitly* penalizing the model for the use of artifactual data, as modeled in latent space, for the prediction of a given class, allowing class-specific corrections.

Note, that shortcut removal by data cleaning, input-level augmentation, or resampling [41, 27, 37, 21] is often insufficient in practice, requiring *full* re-training, where the cleaning process itself either leads to reduced training size, or is impracticably labor-intensive. In this work, we focus on post-hoc model correction based on only few fine-tuning steps.

3 Methods

We present RR-CIArC, a novel method for post-hoc model correction through the latent gradient. As illustrated in Figure 1, our method is based on two steps: (1) computing a robust CAV to model a bias concept, as described in Section 3.1, and (2) bias unlearning by penalizing model sensitivity along the CAV direction, described in Section 3.3.

A feed-forward DNN can be seen as a function $f : \mathcal{X} \rightarrow \mathcal{Y}$, mapping input samples $\mathbf{x} \in \mathcal{X}$ to outputs $y \in \mathcal{Y}$, that is given as a composition of n functions f_i for each layer as

$$f = \underbrace{f_n \circ f_{n-1} \circ \dots \circ f_{l+1}}_{\tilde{f}: \mathbb{R}^m \rightarrow \mathcal{Y}} \circ \underbrace{f_l \circ \dots \circ f_1}_{\mathbf{a}: \mathcal{X} \rightarrow \mathbb{R}^m}. \quad (1)$$

We can further split the model f into two parts as noted in Equation (1): a feature extractor $\mathbf{a} : \mathcal{X} \rightarrow \mathbb{R}^m$ for the latent activations of a chosen layer l (with m neurons), and a model head $\tilde{f} : \mathbb{R}^m \rightarrow \mathcal{Y}$, mapping the activations to the outputs. Note, that the feature extractor \mathbf{a} is used to compute a CAV for modeling bias concepts in latent space.

3.1 Choosing The Right Direction

The authors of [17] define a Concept Activation Vector as the normal to a hyperplane separating samples without a concept and samples with a concept in the model’s latent activations for a selected layer. This hyperplane is commonly computed by solving a classification problem, *e.g.*, using SVMs, ridge, lasso, or logistic regression [17, 26, 2, 39]. We refer to Appendix A.4 for details on optimizer differences. The weight vector resulting from classification solvers, however, are not necessarily ideal CAVs, as the direction best separating two distributions does not always point from one distribution to the other [14]. To that end, signal-pattern-based CAVs (“signal-CAVs”) have been proposed [25], which are more robust against noise.

Concretely, a signal-CAV is given by the correlation between latent activations $\mathbf{a}(\mathbf{x})$ of samples \mathbf{x} and concept labels $t \in \{0, 1\}$ of the concept-labeled dataset $\mathbf{x}, t \in \mathcal{X}_h$ as

$$\mathbf{h}^{\text{signal}} = \sum_{\mathbf{x}, t \in \mathcal{X}_h} (\mathbf{a}(\mathbf{x}) - \bar{\mathbf{a}})(t - \bar{t}) \quad (2)$$

with mean activation $\bar{\mathbf{a}} = \frac{1}{|\mathcal{X}_h|} \sum_{\mathbf{x}, t \in \mathcal{X}_h} \mathbf{a}(\mathbf{x})$ and mean concept label $\bar{t} = \frac{1}{|\mathcal{X}_h|} \sum_{\mathbf{x}, t \in \mathcal{X}_h} t$.

3.2 Class Artifact Compensation

The CIArC framework corrects model (mis-)behavior w.r.t. an artifact by modeling its direction \mathbf{h} in latent

space using CAVs. The framework consists of two methods, namely Augmentive CIArC (CIArC) and Projective CIArC (CIArC). While A-CIArC adds the artifact to activations $\mathbf{a}(\mathbf{x})$ of layer l for all samples in a fine-tuning phase, hence teaching the model to become more invariant towards that direction, P-CIArC suppresses the artifact direction during the test phase and does not require fine-tuning. More precisely, the perturbed activations $\mathbf{a}'(\mathbf{x})$ are given by

$$\mathbf{a}'(\mathbf{x}) = \mathbf{a}(\mathbf{x}) + \gamma(\mathbf{x})\mathbf{h} \quad (3)$$

with perturbation strength $\gamma(\mathbf{x})$ depending on input \mathbf{x} . Here, $\gamma(\mathbf{x})$ is chosen such that the activation in direction of the CAV is as high as the average value over non-artifactual or artifactual samples for P-CIArC or A-CIArC, respectively.

3.3 RR-CIArC: Penalizing the Wrong Reasons

To reduce a DNN’s bias sensitivity, we introduce RR-CIArC, which *explicitly* penalizes the output gradient in the direction of a bias CAV \mathbf{h} . Specifically, RR-CIArC introduces an additional loss term for a fine-tuning step which penalizes the model for using features aligning with the bias direction by computing the inner product between CAV \mathbf{h} (*bias direction*) and the gradient of the output w.r.t. the latent features $\nabla_{\mathbf{a}} \tilde{f}(\mathbf{a}(\mathbf{x}))$ (*sensitivity w.r.t. latent features*), given by

$$L_{\text{RR}}(\mathbf{x}) = \left(\nabla_{\mathbf{a}} \tilde{f}(\mathbf{a}(\mathbf{x})) \cdot \mathbf{h} \right)^2. \quad (4)$$

To enable a class-specific bias unlearning for models with k (multiple) output classes, described by function $\mathbf{f}(\mathbf{x}) \in \mathbb{R}^k$, we extend the loss term to

$$L_{\text{RR}}(\mathbf{x}) = \left(\nabla_{\mathbf{a}} \left[\mathbf{m} \cdot \tilde{\mathbf{f}}(\mathbf{a}(\mathbf{x})) \right] \cdot \mathbf{h} \right)^2 \quad (5)$$

where the regularization can be controlled class-specifically with annotation vector $\mathbf{m} \in \mathbb{R}^k$. For regularizing all classes, we can set all elements of \mathbf{m} to one. However, choosing elements uniformly randomly as $(\mathbf{m})_i \in_R \{-1, 1\}$ for each sample \mathbf{x} improves regularization, further motivated in Appendix E. Alternatively, we can also correct for a specific class c by choosing $(\mathbf{m})_i = \delta_{ic}$ with Kronecker-delta δ , which ensures that related (harmless) concepts relevant for other classes are not unlearned (see Section 4.4).

Intuitively, the loss L_{RR} penalizes the model for changing the output when slightly adding or removing activations along the bias direction \mathbf{h} , *i.e.*

$$\lim_{\epsilon \rightarrow 0} \frac{\tilde{f}(\mathbf{a}(\mathbf{x}) + \epsilon \mathbf{h}) - \tilde{f}(\mathbf{a}(\mathbf{x}))}{\epsilon} \approx \nabla_{\mathbf{a}} \tilde{f}(\mathbf{a}(\mathbf{x})) \cdot \mathbf{h} \stackrel{!}{=} 0. \quad (6)$$

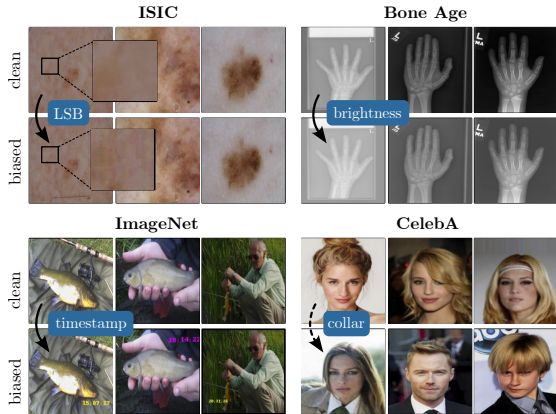


Figure 2: Overview of investigated data biases. (Top left): Samples of the ISIC dataset are corrupted using an LSB attack. (Top right): The brightness of samples from the Bone Age dataset is increased. (Bottom left): An artificial timestamp is added to samples from ImageNet. (Bottom right): The CelebA dataset intrinsically has a negative correlation between the existence of collars and blonde hair.

Thus, by minimizing L_{RR} , the model becomes insensitive towards the bias direction. Note, that in order to ensure that the bias direction \mathbf{h} in layer l stays constant, all weights of layers $l' \leq l$ need to be frozen during the fine-tuning phase.

4 Experiments

Our experiments aim to answer the following questions:

- (Q1) How well do CAVs computed with typical approaches align with the true bias direction?
- (Q2) How effective does RR-ClArC revise biases compared to other state-of-the-art methods?
- (Q3) Is RR-ClArC suitable for class-specific unlearning?
- (Q4) How does each component of RR-ClArC affect its performance?

4.1 Experimental Setting

Datasets and Models

We fine-tune pre-trained VGG-16 [32], ResNet-18 [15] and EfficientNet-B0 [33] models on the ISIC 2019 dataset [7, 36, 8] for skin lesion classification, the Pediatric Bone Age dataset [13] for bone age estimation based on hand radiographs, ImageNet [11] for large scale visual recognition, and the CelebA dataset [22], offering face attributes of celebrities with the task to predict hair color. For the former three datasets, we artificially insert ‘‘Clever Hans’’

artifacts, *i.e.*, features unrelated to the given task, yet correlating with the target class, into data samples from only one class in a controlled setting, encouraging the model to learn a shortcut. Specifically, we use two spatially unlocalized artifacts, by (1) increasing the image brightness, *i.e.*, increasing pixel values for each color channel, for the Bone Age dataset, and (2), run a least significant bit (LSB) attack on ISIC 2019. Inspired by steganography techniques, LSB attacks hide secret messages, *e.g.*, a text message converted into a bit stream, into the least significant bits of input features (here: voxel values) of the DNN [20], which is hardly visible to the human eye. For ImageNet, we insert a timestamp to images, mimicking the option of digital cameras to add time information via text overlay. Lastly, for CelebA, we leverage a dataset-intrinsic bias, namely the negative correlation of the existence of collars and blonde hair, which is picked up by models to predict hair color (see Figure 1). An overview of the data artifacts is provided in Figure 2. All datasets are split into training, validation, and test sets. Additional dataset and training details are provided in Appendix A.

Concept Activation Vectors

To compute CAVs, the last convolutional layer is chosen for all models to extract features $\mathbf{a}(\mathbf{x})$, most likely representing disentangled representations [40]. We tune hyperparameters γ as $\gamma \in \{10^{-5}, 10^{-4}, \dots, 10^5\}$ for all regression-based optimizers. Further details are given in Appendix A.

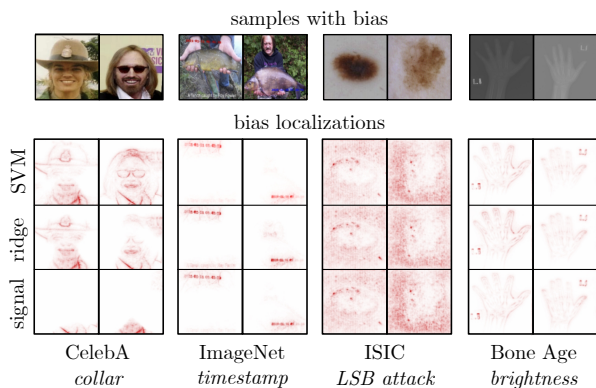
4.2 CAV Alignment With True Direction (Q1)

A CAV, modeling an artifact, ideally represents the direction in latent activation space pointing from a cluster of clean samples to a cluster of artifactual samples. However, the alignment between CAV and (usually unknown) concept direction is often not evaluated. In the following, we illustrate a qualitative and quantitative approach to assess CAVs, and identify shortcomings of regression-based CAV optimizers.

Qualitative Alignment

To bridge the gap between latent activation space and human-interpretable input space, we follow [2, 24], and localize our biases in the input image based on CAVs. Such localization can be achieved by computing an attribution heatmap, not w.r.t. to the output logit as for standard explanation heatmaps, but w.r.t. the dot-product between CAV and activations, *i.e.*, $\mathbf{a} \cdot \mathbf{h}$. All computed heatmaps are based on the LRP attribution method [3]

a qualitative evaluation of CAV alignment



b quantitative evaluation of CAV alignment

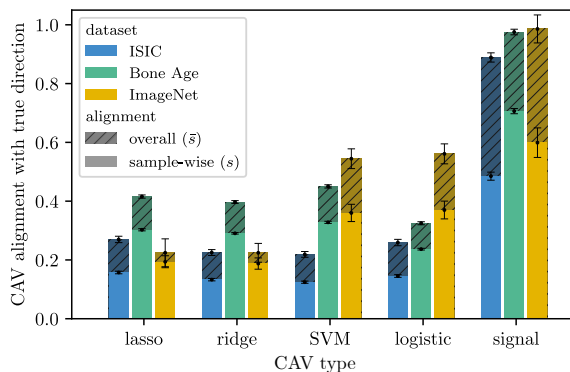


Figure 3: Evaluating CAV alignments. **a)** CAV localization heatmaps allow to qualitatively check the alignment of a CAV with a concept. Whereas the signal-CAV tends to pinpoint the bias best for CelebA, all CAV types similarly highlight the biases of the ImageNet, ISIC, Bone Age dataset. **b)** In the controlled settings, we can compute the *true* alignment with the modeled CAV by measuring the change in activations when the bias concept is added to the input. Here, signal-CAV leads to significantly better alignments than other commonly used regression-based approaches, such as SVM-CAV in *all* experiments. This indicates, that sensible CAV localizations do not necessitate a high alignment. The Standard Error of the Mean (SEM) is shown by error bars. Best viewed digitally.

with the $\varepsilon z^+ b$ -composite [18], as implemented in the zennit [1] package.

Examples of bias localization heatmaps using signal, ridge and SVM-CAVs are shown in Figure 3a for all experimental datasets with VGG-16. For the CelebA dataset, signal-CAVs tend to pinpoint the collar bias best, with ridge and SVM also highlighting unrelated features. Regarding ImageNet and the unlocalized biases (ISIC, Bone Age), all CAV types highlight bias features. Here, no difference between CAV types is apparent. More bias localizations are provided in Appendix B. Note, however, that a good agreement in localization does not necessitate good alignment, as the quantitative evaluation in the following section shows.

Quantitative Alignment

In order to measure to which degree a bias CAV corresponds to the true direction in the latent space, we perform experiments in a controlled setting (ISIC, ImageNet, Bone Age). Specifically, we apply an input transformation φ that adds the bias to the input as $\varphi(\mathbf{x}) = \tilde{\mathbf{x}}$, and measure the cosine similarity between the bias CAV and the resulting difference in activations $\Delta \mathbf{a}(\mathbf{x}) = \mathbf{a}(\tilde{\mathbf{x}}) - \mathbf{a}(\mathbf{x})$. The alignment s of CAV \mathbf{h} is then given as

$$s = \frac{1}{|\mathcal{X}|} \sum_{\mathbf{x} \in \mathcal{X}} \frac{\mathbf{h} \cdot \Delta \mathbf{a}(\mathbf{x})}{\|\mathbf{h}\|_2 \|\Delta \mathbf{a}(\mathbf{x})\|_2}, \quad (7)$$

where the alignment is computed w.r.t. to the activation difference in *each* sample of dataset \mathcal{X} . Alternatively, we

also compute the overall alignment \bar{s} given by

$$\bar{s} = \frac{\mathbf{h}}{\|\mathbf{h}\|_2} \cdot \frac{\frac{1}{|\mathcal{X}|} \sum_{\mathbf{x} \in \mathcal{X}} \Delta \mathbf{a}(\mathbf{x})}{\left\| \frac{1}{|\mathcal{X}|} \sum_{\mathbf{x}' \in \mathcal{X}} \Delta \mathbf{a}(\mathbf{x}') \right\|_2}, \quad (8)$$

which describes how well the CAV aligns with the mean activation change over *all* samples.

The resulting alignment scores are shown in Figure 3b for the VGG-16 model and the ISIC, ImageNet and Bone Age datasets. Here, we compare CAVs computed through SVM, ridge, lasso and logistic regression as well as correlation (signal). It is apparent, that signal-CAVs perform significantly better than the other approaches, resulting in overall alignments \bar{s} of over 90 % compared to less than 60 % for the regression CAVs. Also, for the sample-wise alignment s , signal-CAVs often shows twice as high alignment scores as other approaches. For EfficientNet and ResNet, similar results can be observed, as shown in Appendix B.

The sample-wise alignment s is generally smaller than the overall alignment. We find that transformation φ barely affects samples in some cases, *e.g.*, when adding a black timestamp to a dark background (ImageNet), leading to low alignments s . We show samples with high and low alignment for all experiments in Appendix Figure A.3.

All in all, the qualitative and quantitative CAV evaluations show, that the CAV optimizer can have a significant impact on the alignment, with regression-based optimizers showing diverging directions. Sensible bias localizations may hint at diverging directions, but do not necessitate good alignment, underlined by the quantitative evalu-

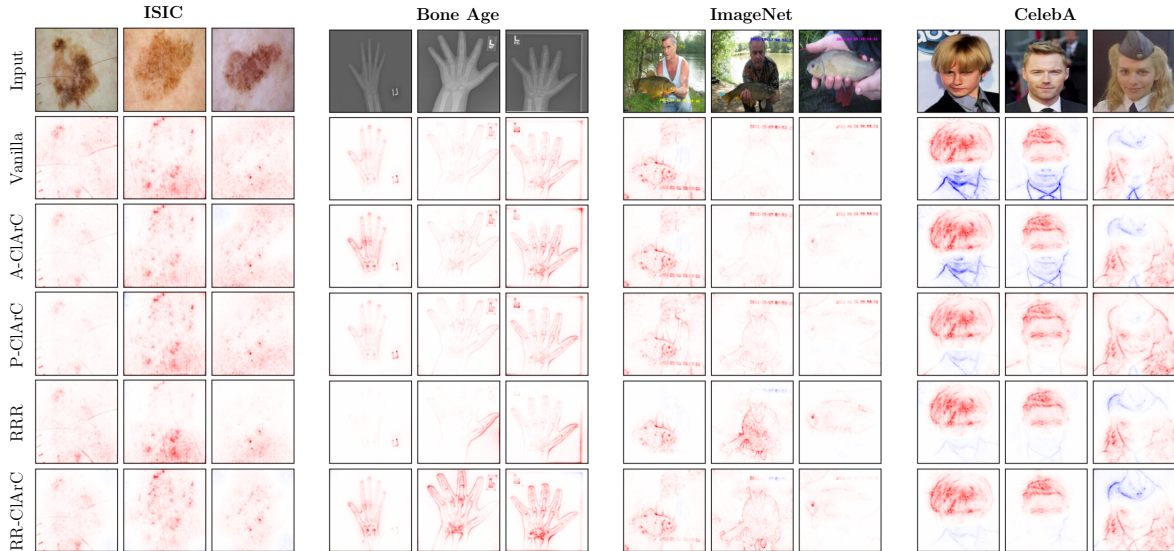


Figure 4: Effect of model correction on explanation heatmaps for the VGG-16 model on all datasets. Whereas RRR successfully decreases the relevance on localized biases (ImageNet and CelebA), RRR tends to fail on unlocalized artifacts (ISIC, Bone Age), with the model’s attention focusing on arbitrary features. Overall, RR-CIArC reduces bias attention most reliably. Best viewed digitally.

ation.

4.3 Revising Model Biases (Q2)

We revise model biases by applying the methods of A- and P-CIArC, the input-level correction method RRR, as well as our introduced method RR-CIArC, and compare with a *Vanilla* model. All models are fine-tuned for 10 epochs. Although not requiring further training, before the application of P-CIArC we fine-tune the model in *Vanilla* fashion for better comparability. For RRR and RR-CIArC, we test different regularization strengths λ , detailed in Appendix A.3. As RRR requires prior input-level bias localizations, we use a threshold to convert artifact localizations retrieved as described in Section 4.2 into binary masks for CelebA. In the controlled experiments, we generate ground truth binary masks to localize inserted artifacts. For unlocalized artifacts (spreading over the entire input) ground truth masks cover the full image. We use signal-CAVs to represent artifacts in latent space for CIArC-methods, as they have shown the best alignment scores in Section 4.2. We fine-tune models using the training set, choose optimal λ values using the validation set, and measure the accuracy on a *clean* and a *biased* test set. While we insert the Clever Hans artifact into all samples from the *biased* test set in the controlled setting, for CelebA we use a subset from the original test set with samples containing the collar-artifact.

Moreover, we measure the remaining sensitivity on the

bias in latent space via TCAV [17], given as

$$\text{TCAV} = \frac{\left| \left\{ \mathbf{x} \in \mathcal{X}_{\text{bias}} : \nabla_{\mathbf{a}} \tilde{f}(\mathbf{a}(\mathbf{x})) \cdot \mathbf{h} > 0 \right\} \right|}{|\mathcal{X}_{\text{bias}}|} \quad (9)$$

computed over the set of all bias samples $\mathcal{X}_{\text{bias}}$. For a bias-insensitive model, we expect $\text{TCAV} \approx 0.5$, describing a random bias impact. For a positively or negatively contributing bias, we expect $\text{TCAV} > 0.5$ or $\text{TCAV} < 0.5$, respectively.

Results The results for all architectures and datasets are shown in Table 1, with respective standard errors given in Appendix C. Across all experiments, RR-CIArC outperforms all competitors on the *biased* test set in terms of accuracy, while not significantly hurting the classification performance on the *clean* test set. Here, RR-CIArC shows the best tradeoff between accuracy on clean and biased data. Note, that an accuracy drop on the clean test set can be expected, as the bias concept might be (partially) entangled with sensible related concepts in latent space, which, consequently, are suppressed during unlearning as well. However, in principle, the clean accuracy could also increase when alternative strategies based on other features are found.

Notably, RRR increases the biased test set accuracy only for localized biases effectively (ImageNet, CelebA). This is expected, as input localizations for unlocalized biases cover the full image (including sensible features), and

Table 1: Model correction results for all experiments. We report model accuracy (in %) on *clean* and *biased* test sets, as well as TCAV bias score. Higher scores are better for accuracy and scores close to 0.5 are best for TCAV, with best scores bold.

architecture	method	Bone Age			ISIC			ImageNet			CelebA		
		<i>clean</i>	<i>biased</i>	TCAV									
VGG-16	<i>Vanilla</i>	78.8	49.8	0.86	76.2	34.9	0.84	68.7	43.5	0.63	93.7	82.8	0.37
	RRR	78.8	49.8	0.86	76.7	42.8	0.72	68.6	49.6	0.55	93.7	91.2	0.43
	P-CIArC	78.9	77.4	0.66	75.1	49.0	0.77	68.3	62.6	0.37	56.6	60.8	0.19
	A-CIArC	77.8	69.0	0.66	75.2	49.5	0.65	67.7	60.9	0.49	93.0	90.4	0.44
	RR-CIArC (ours)	78.8	77.7	0.52	74.3	57.0	0.49	68.5	62.6	0.49	93.6	92.6	0.54
ResNet-18	<i>Vanilla</i>	75.1	46.3	1.00	81.8	56.8	1.00	66.7	52.9	1.00	96.8	58.3	0.21
	RRR	74.5	47.9	1.00	78.7	61.1	1.00	66.4	59.1	0.08	95.5	74.7	0.92
	P-CIArC	75.0	70.7	0.60	60.8	59.9	1.00	67.0	61.7	0.80	96.5	64.4	0.06
	A-CIArC	74.8	57.4	0.34	77.1	65.0	0.98	65.0	63.3	0.88	96.1	62.9	0.38
	RR-CIArC (ours)	71.1	74.2	0.39	78.5	71.2	0.76	66.5	64.0	0.55	95.8	75.3	0.61
Efficient Net-B0	<i>Vanilla</i>	78.2	44.3	0.90	84.2	62.9	1.00	73.9	53.2	0.99	96.6	58.3	0.25
	RRR	78.4	49.6	0.79	83.1	68.7	0.85	73.9	59.1	0.66	95.4	75.6	0.50
	P-CIArC	65.2	35.1	0.02	19.7	29.6	1.00	74.1	54.6	0.21	96.8	55.0	0.05
	A-CIArC	78.0	54.2	0.64	77.7	72.8	0.68	71.4	69.9	0.90	96.7	60.6	0.24
	RR-CIArC (ours)	77.6	70.3	0.53	78.7	75.6	0.54	73.9	70.8	0.56	92.0	77.6	0.43

thus tend to steer the models’ attention towards sparse, but (possibly) insensible features. Our findings are supported by qualitative results in Figure 4, showing LRP explanation heatmaps for the corrected and Vanilla models. While the Vanilla models show large fractions of relevance on the biases (background for unlocalized artifacts), RR-CIArC performs best in teaching the model to solely focus on the object of interest, which RRR can only achieve for the localized artifacts.

Whereas CIArC-methods operating in latent activation space show reasonable accuracy gains in comparison with the Vanilla model for most tasks, they mostly only slightly decrease bias sensitivity. RR-CIArC yields better results for TCAV, *i.e.* $TCAV \approx 0.5$, due to the explicit penalization of bias sensitivity in latent space, as described in Equation (5). Note, that TCAV only takes into account the sign of bias sensitivity, not the magnitude. To that end, we further report bias sensitivity magnitudes in Appendix C, and alternatively, also report input-level bias relevances for localized artifacts.

Overall, RR-CIArC yields the most reliable results, recovering the classification performance on biased datasets for both localized and unlocalized artifacts, while strongly decreasing bias sensitivity and remaining predictive performance on the clean test set.

Computational Cost

By performing a single forward pass per sample, A-CIArC is as computationally expensive as Vanilla training. RR-CIArC increases training time for the VGG-16 model by about 20 % due to, *e.g.*, additionally requiring a partial

backward pass (up to the CAV layer) to compute the latent gradient for the loss. RRR is most expensive with a time increase of about 73 % for VGG-16, requiring both a full forward and backward pass to compute the loss. Note, that P-CIArC does not require fine-tuning. Exact training times are given in Table A.6 of the Appendix.

4.4 Class-specific Model Correction (Q3)

Another advantage of RR-CIArC in comparison to other CIArC methods is its ability to correct model behavior w.r.t. bias concepts for *specific* classes by specifying annotation vector \mathbf{m} in Equation 5 accordingly, penalizing the gradient only for chosen classes. This allows to teach the model to ignore concepts, *e.g.*, the timestamp artifact (ImageNet), for a specific class (here: “tench”), while allowing other classes such as, *e.g.*, “digital clock”, to rely on related concepts.

In this experiment, we study the impact of model corrections on model accuracy w.r.t. classes using concepts related to the timestamp bias. A *selected* subset of related classes is identified by a strong increase in their output logit when adding a timestamp to the input, listed in Appendix D. We then compare the impact of model corrections on the accuracy for clean samples between the *selected* classes and *all* classes. The change in accuracies for VGG-16 corrections in comparison with the Vanilla model is shown in Figure 5, and for other architectures in Appendix D. As expected, A- and P-CIArC lead to a significant drop in accuracy for the *selected* classes, confirming that the model suppressed related concepts required

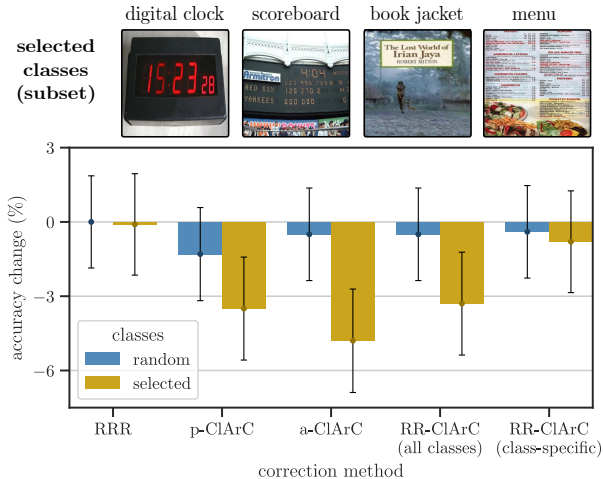


Figure 5: Impact of model correction for the timestamp bias (ImageNet) on model accuracy for random and selected classes (*bottom*), where selected classes are highly impacted by the timestamp bias, *e.g.*, “digital clock” (*top*). While A-CIArC and P-CIArC are class-inspecific and lead to a drop in accuracy for selected classes, RRR and RR-CIArC *only* unlearn the artifact for a specific class. Note, that RR-CIArC can target both, all classes or specific classes.

to recognize these classes. RRR and RR-CIArC, however, targeting the “tench” class only through the gradient, retain the model’s accuracy for the *selected* classes. Note, that RR-CIArC can also target *all* classes, showing similar results as A- and P-CIArC then.

4.5 Ablation Study (Q4)

The following ablation study measures the impact of the main influencing factors of RR-CIArC, including the choice of CAV optimizer and regularization strength. Other factors, including the number of fine-tuning epochs and the choice of the target w.r.t. which the gradient is computed as in Equation (5), are discussed in Appendix E.

Concept Activation Vector

When comparing the accuracy on the biased test set after model correction with RR-CIArC using different CAV optimizers, signal-CAVs significantly outperform all competitors, as shown in Figure 6 for the VGG-16 model with controlled biases. This follows the trend in the alignment experiment of Section 4.2, confirming that a high CAV alignment is required to effectively regularize all parts of a concept to fully unlearn harmful concepts.

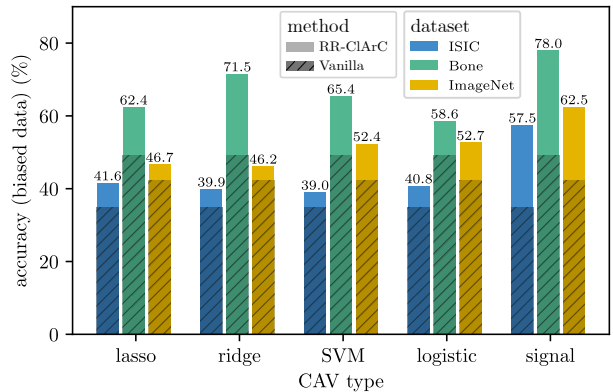


Figure 6: On all experiments, the CAV type has a significant impact on model correction (regarding accuracy on the biased dataset), with signal-CAV leading to the highest accuracies (Standard Error (SE) less than 1%). These results mirror the CAV alignment experiment in Figure 3b.

Regularization Strength

Besides CAV type, the regularization strength λ is another important parameter controlling the amount of unlearning. The higher λ , the higher the accuracy on the biased dataset up to a turning point, when the regularization becomes too strong, and the overall accuracy is reduced again, also shown in Figure A.18 of the Appendix. When a CAV is not perfectly aligned, or the bias concept entangled with useful directions in the latent space, strong regularization can be expected to harm performance.

5 Conclusion

We present RR-CIArC, a post-hoc model correction method based on CAVs and the latent gradient. RR-CIArC is a step towards easier and more generalized model correction requiring only sparse labels to unlearn any concept (unlocalized or localized) class-specifically, and being applicable to any DNN architecture with access to latent features. Throughout experiments with three popular DNN architectures on four datasets with controlled and data-intrinsic biases, RR-CIArC unlearns biases most effectively and consistently compared to other state-of-the-art approaches. In our experiments, we find that Concept Activation Vectors, which are usually applied to model latent concepts, tend to result in diverging directions when based on popular regression-based approaches such as, *e.g.*, SVMs. An important future direction will be to investigate these shortcomings further, with the possibility to improve concept-based methods in various applications.

Limitations RR-CIArC requires the freezing of layers from input to the feature layer where the bias-CAV is

modeled. However, in principle, a subsequent fine-tuning step without freezing parameters on clean data is possible. Moreover, our experiments show that a well-aligned CAV is necessary for effective bias unlearning. Choosing the last convolutional layer for modeling CAVs might not always be optimal. It is still an open question, how to choose the optimal layer for bias correction.

Acknowledgements

This work was supported by the Federal Ministry of Education and Research (BMBF) as grant BIFOLD (01IS18025A, 01IS180371I); the German Research Foundation (DFG) as research unit DeSbi (KI-FOR 5363); the European Union’s Horizon Europe research and innovation programme (EU Horizon Europe) as grant TEMA (101093003); the European Union’s Horizon 2020 research and innovation programme (EU Horizon 2020) as grant iToBoS (965221); and the state of Berlin within the innovation support programme ProFIT (IBB) as grant BerDiBa (10174498).

References

- [1] Christopher J. Anders, David Neumann, Wojciech Samek, Klaus-Robert Müller, and Sebastian Lapuschkin. Software for dataset-wide xai: From local explanations to global insights with Zennit, CoReLay, and ViRelAy, 2021.
- [2] Christopher J Anders, Leander Weber, David Neumann, Wojciech Samek, Klaus-Robert Müller, and Sebastian Lapuschkin. Finding and removing clever hans: Using explanation methods to debug and improve deep models. *Information Fusion*, 77:261–295, 2022.
- [3] Sebastian Bach, Alexander Binder, Grégoire Montavon, Frederick Klauschen, Klaus-Robert Müller, and Wojciech Samek. On pixel-wise explanations for non-linear classifier decisions by layer-wise relevance propagation. *PloS one*, 10(7):e0130140, 2015.
- [4] Andrea Bontempelli, Stefano Teso, Fausto Giunchiglia, and Andrea Passerini. Concept-level debugging of part-prototype networks. In *Workshop on Trustworthy Artificial Intelligence as a part of the ECML/PKDD 22 program*, 2022.
- [5] Kirill Bykov, Mayukh Deb, Dennis Grinwald, Klaus Robert Muller, and Marina MC Höhne. Dora: Exploring outlier representations in deep neural networks. In *ICLR 2023 Workshop on Pitfalls of limited data and computation for Trustworthy ML*, 2023.
- [6] Bill Cassidy, Connah Kendrick, Andrzej Brodzicki, Joanna Jaworek-Korjakowska, and Moi Hoon Yap. Analysis of the isic image datasets: Usage, benchmarks and recommendations. *Medical image analysis*, 75:102305, 2022.
- [7] Noel CF Codella, David Gutman, M Emre Celebi, Brian Helba, Michael A Marchetti, Stephen W Dusza, Aadi Kallou, Konstantinos Liopyris, Nabin Mishra, Harald Kittler, et al. Skin lesion analysis toward melanoma detection: A challenge at the 2017 international symposium on biomedical imaging (isbi), hosted by the international skin imaging collaboration (isic). In *15th International Symposium on Biomedical Imaging (ISBI 2018)*, pages 168–172. IEEE, 2018.
- [8] Marc Combalia, Noel CF Codella, Veronica Rotemberg, Brian Helba, Veronica Vilaplana, Ofer Reiter, Cristina Carrera, Alicia Barreiro, Allan C Halpern, Susana Puig, et al. Bcn20000: Dermoscopic lesions in the wild, 2019.
- [9] Corinna Cortes and Vladimir Vapnik. Support-vector networks. *Machine learning*, 20:273–297, 1995.
- [10] Alex J DeGrave, Joseph D Janizek, and Su-In Lee. Ai for radiographic covid-19 detection selects shortcuts over signal. *Nature Machine Intelligence*, 3(7):610–619, 2021.
- [11] Jia Deng, Wei Dong, Richard Socher, Li-Jia Li, Kai Li, and Li Fei-Fei. Imagenet: A large-scale hierarchical image database. In *IEEE conference on computer vision and pattern recognition*, pages 248–255. IEEE, 2009.
- [12] Robert Geirhos, Jörn-Henrik Jacobsen, Claudio Michaelis, Richard Zemel, Wieland Brendel, Matthias Bethge, and Felix A Wichmann. Shortcut learning in deep neural networks. *Nature Machine Intelligence*, 2(11):665–673, 2020.
- [13] Safwan S Halabi, Luciano M Prevedello, Jayashree Kalpathy-Cramer, Artem B Mamonov, Alexander Bilbily, Mark Cicero, Ian Pan, Lucas Araújo Pereira, Rafael Teixeira Sousa, Nitamar Abdala, et al. The rsna pediatric bone age machine learning challenge. *Radiology*, 290(2):498–503, 2019.
- [14] Stefan Haufe, Frank Meinecke, Kai Görden, Sven Dähne, John-Dylan Haynes, Benjamin Blankertz, and Felix Bießmann. On the interpretation of weight vectors of linear models in multivariate neuroimaging. *Neuroimage*, 87:96–110, 2014.

- [15] Kaiming He, Xiangyu Zhang, Shaoqing Ren, and Jian Sun. Deep residual learning for image recognition. In *Proceedings of the IEEE Conference on Computer Vision and Pattern Recognition*, pages 770–778, 2016.
- [16] Arthur E Hoerl and Robert W Kennard. Ridge regression: Biased estimation for nonorthogonal problems. *Technometrics*, 12(1):55–67, 1970.
- [17] Been Kim, Martin Wattenberg, Justin Gilmer, Carrie Cai, James Wexler, Fernanda Viegas, et al. Interpretability beyond feature attribution: Quantitative testing with concept activation vectors (tcav). In *International Conference on Machine Learning*, pages 2668–2677. PMLR, 2018.
- [18] Maximilian Kohlbrenner, Alexander Bauer, Shinichi Nakajima, Alexander Binder, Wojciech Samek, and Sebastian Lapuschkin. Towards best practice in explaining neural network decisions with lrp. In *2020 International Joint Conference on Neural Networks (IJCNN)*, pages 1–7. IEEE, 2020.
- [19] Sebastian Lapuschkin, Stephan Wäldchen, Alexander Binder, Grégoire Montavon, Wojciech Samek, and Klaus-Robert Müller. Unmasking clever hans predictors and assessing what machines really learn. *Nature Communications*, 10(1):1096, 2019.
- [20] Shaofeng Li, Minhui Xue, Benjamin Zi Hao Zhao, Haojin Zhu, and Xinpeng Zhang. Invisible backdoor attacks on deep neural networks via steganography and regularization. *IEEE Transactions on Dependable and Secure Computing*, 18(5):2088–2105, 2020.
- [21] Zhiheng Li, Ivan Evtimov, Albert Gordo, Caner Hazirbas, Tal Hassner, Cristian Canton Ferrer, Chenliang Xu, and Mark Ibrahim. A whac-a-mole dilemma: Shortcuts come in multiples where mitigating one amplifies others. In *Proceedings of the IEEE/CVF Conference on Computer Vision and Pattern Recognition*, pages 20071–20082, 2023.
- [22] Ziwei Liu, Ping Luo, Xiaogang Wang, and Xiaoou Tang. Deep learning face attributes in the wild. In *Proceedings of International Conference on Computer Vision (ICCV)*, December 2015.
- [23] Maggie Makar, Ben Packer, Dan Moldovan, Davis Blalock, Yoni Halpern, and Alexander D’Amour. Causally motivated shortcut removal using auxiliary labels. In *International Conference on Artificial Intelligence and Statistics*, pages 739–766. PMLR, 2022.
- [24] Frederik Pahde, Maximilian Dreyer, Wojciech Samek, and Sebastian Lapuschkin. Reveal to revise: An explainable AI life cycle for iterative bias correction of deep models. In Hayit Greenspan, Anant Madabhushi, Parvin Mousavi, Septimiu Salcudean, James Duncan, Tanveer F. Syeda-Mahmood, and Russell H. Taylor, editors, *Medical Image Computing and Computer Assisted Intervention - MICCAI 2023 - 26th International Conference, Proceedings, Part II*, volume 14221 of *Lecture Notes in Computer Science*, pages 596–606. Springer, 2023.
- [25] Frederik Pahde, Leander Weber, Christopher J Anders, Wojciech Samek, and Sebastian Lapuschkin. Patclarc: Using pattern concept activation vectors for noise-robust model debugging, 2022.
- [26] Jacob Pfau, Albert T Young, Jerome Wei, Maria L Wei, and Michael J Keiser. Robust semantic interpretability: Revisiting concept activation vectors, 2021.
- [27] Gregory Plumb, Marco Túlio Ribeiro, and Ameet Talwalkar. Finding and fixing spurious patterns with explanations. *Transactions on Machine Learning Research*, 2022, 2022.
- [28] Laura Rieger, Chandan Singh, William Murdoch, and Bin Yu. Interpretations are useful: penalizing explanations to align neural networks with prior knowledge. In *International Conference on Machine Learning*, pages 8116–8126. PMLR, 2020.
- [29] Joshua Robinson, Li Sun, Ke Yu, Kayhan Batmanghelich, Stefanie Jegelka, and Suvrit Sra. Can contrastive learning avoid shortcut solutions? *Advances in neural information processing systems*, 34:4974–4986, 2021.
- [30] Andrew Slavin Ross, Michael C Hughes, and Finale Doshi-Velez. Right for the right reasons: training differentiable models by constraining their explanations. In *Proceedings of the 26th International Joint Conference on Artificial Intelligence*, pages 2662–2670, 2017.
- [31] Patrick Schramowski, Wolfgang Stammer, Stefano Teso, Anna Brugger, Franziska Herbert, Xiaoting Shao, Hans-Georg Luigs, Anne-Katrin Mahlein, and Kristian Kersting. Making deep neural networks right for the right scientific reasons by interacting with their explanations. *Nature Machine Intelligence*, 2(8):476–486, 2020.
- [32] Karen Simonyan and Andrew Zisserman. Very deep convolutional networks for large-scale image recognition. In Yoshua Bengio and Yann LeCun, editors,

International Conference on Learning Representations, ICLR 2015, 2015.

- [33] Mingxing Tan and Quoc Le. Efficientnet: Rethinking model scaling for convolutional neural networks. In *International Conference on Machine Learning*, pages 6105–6114. PMLR, 2019.
- [34] Stefano Teso and Kristian Kersting. Explanatory interactive machine learning. In *Proceedings of the 2019 AAAI/ACM Conference on AI, Ethics, and Society*, pages 239–245, 2019.
- [35] Robert Tibshirani. Regression shrinkage and selection via the lasso. *Journal of the Royal Statistical Society Series B: Statistical Methodology*, 58(1):267–288, 1996.
- [36] Philipp Tschandl, Cliff Rosendahl, and Harald Kittler. The ham10000 dataset, a large collection of multi-source dermatoscopic images of common pigmented skin lesions. *Scientific data*, 5(1):1–9, 2018.
- [37] Shirley Wu, Mert Yuksekgonul, Linjun Zhang, and James Zou. Discover and cure: Concept-aware mitigation of spurious correlation. In *International Conference on Machine Learning*, 2023.
- [38] Siyuan Yan, Zhen Yu, Xuelin Zhang, Dwarikanath Mahapatra, Shekhar S Chandra, Monika Janda, Peter Soyer, and Zongyuan Ge. Towards trustable skin cancer diagnosis via rewriting model’s decision. In *Proceedings of the IEEE/CVF Conference on Computer Vision and Pattern Recognition*, pages 11568–11577, 2023.
- [39] Mert Yuksekgonul, Maggie Wang, and James Zou. Post-hoc concept bottleneck models. In *The Eleventh International Conference on Learning Representations*, 2023.
- [40] Matthew D Zeiler and Rob Fergus. Visualizing and understanding convolutional networks. In *Computer Vision – ECCV 2014*, pages 818–833. Springer, 2014.
- [41] Hongyi Zhang, Moustapha Cisse, Yann N Dauphin, and David Lopez-Paz. mixup: Beyond empirical risk minimization. In *International Conference on Learning Representations*, 2018.

Appendix

A Experiment Details

In the following, we provide more details regarding our experimental settings.

A.1 Datasets

Additional details for the datasets considered in our experiments are given in Table A.1. Specifically, we list the artifact type, whether the artifact is controlled or dataset-intrinsic, the number of samples, the number of output classes, the biased class containing the artifact, the percentage of samples in that class containing the artifact (p-bias), as well as the training/validation/test split for the Bone Age, ISIC2019, ImageNet, and CelebA datasets. Note, that the model architectures considered in our experiments differ in their sensitivity towards investigated artifacts. For that reason, we use different values for p-bias by artifact type and model architecture. Moreover, for the LSB attack on the ISIC2019 dataset, we vary the number of least significant bits to be overwritten, namely 3/3/2 bits for VGG-16, ResNet-18, and EfficientNet-B0, respectively. A visualization for the LSB attack on ISIC2019 samples is shown in Figure A.1. For the Bone Age dataset, we convert the regression task into a classification task by binning the age into 5 equal-width bins. The artifact function π increasing the brightness of the image updates voxel values $v \in [0, 255]$ as $\pi(v) = \min(255, (1 - \alpha) \cdot v + \alpha \cdot 255)$ with $\alpha = 0.3$. To artificially increase the sensitivity of the models to the timestamp artifact in ImageNet, in addition to the 50% Clever Hans samples in the class “tench”, we randomly insert the artifact into 0.1% of samples from *all* classes and flip the label to “tench” during training. Furthermore, we use the default ImageNet validation set as test set and split the training set into our training and validation sets, resulting in a train/val/test split distribution of approximately 86%/10%/4%. For CelebA, we only use a subset of the data, by selecting 10% of all samples and adding all remaining samples with the “wearing_necktie”-attribute, totaling to 33,480 samples. We use a binary target label based on the attribute “blonde_hair”.

A.2 Model Training

In our experiments, we train VGG-16, ResNet-18, and EfficientNet-B0 models with optimizer, loss function, learning rate, and number of epochs as specified in Table A.2. We divide the learning rate by 10 after 30/40 (ISIC2019, Bone Age) and 20/30 (CelebA) epochs, respectively. All models were pre-trained on ImageNet and downloaded from the PyTorch model zoo. Whereas for

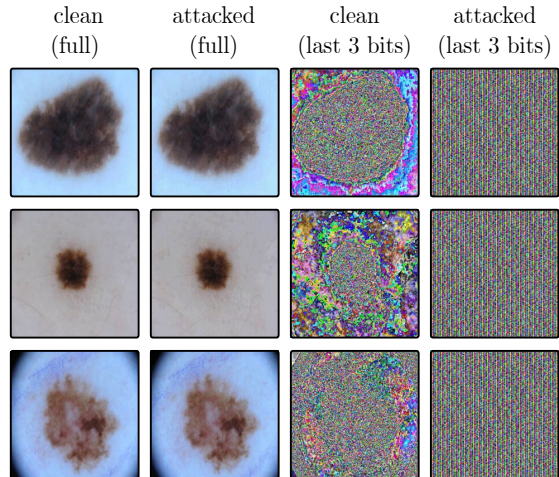


Figure A.1: Visualization of the LSB attack on samples from ISIC2019. *From left to right:* (1) Clean samples, (2) attacked samples, (3) only the last 3 bits from pixel values of clean samples, and (4) the last 3 bits of attacked samples. While full clean and attacked samples are barely distinguishable by the human eye, only visualizing the last 3 bits reveals the message encoded into attacked samples. Note, that the stripe-pattern comes from the fact that for characters considered for the message (a-z), all ASCII byte representations start with the identical 3 bits. This, in conjunction with the fact that we re-size images to size 224×224 , *i.e.*, a multiple of 8, leads to the stripes in the shown representation.

Bone Age, ISIC2019, and CelebA we used the same number of epochs for all models, we used different checkpoints for ImageNet because models reacted at varying speeds to the artifact (as measured on the validation set).

A.3 Model Correction

For model correction, all models, including *Vanilla*, are fine-tuned for 10 epochs. We use the same loss function and optimizer as for training, *i.e.*, cross-entropy loss and SGD (VGG-16, ResNet-18) and Adam (EfficientNet-B0) optimizers, but with reduced learning rate. Specifically, we use 10^{-4} as learning rate for all model correction runs, except for ResNet-18 runs for CelebA, where we use $2 \cdot 10^{-5}$, because we observed more stable results on the validation set. For RRR and RR-CIArC we tested $\lambda \in \{5 \cdot 10^{-5}, 10^{-3}, 5 \cdot 10^{-3}, 10^{-2}, \dots, 10^6, 5 \cdot 10^6, 10^7\}$ and $\lambda \in \{5 \cdot 10^1, 10^2, 5 \cdot 10^2, 10^3, \dots, 10^{11}, 5 \cdot 10^{11}, 10^{12}\}$, respectively. Best performing λ values, as measured on the validation sets, are shown in Table A.3.

Table A.1: Details for datasets considered in our experiments, namely Bone Age, ISIC2019, ImageNet, and CelebA. Note, that for CelebA, we only use a subset of samples (33,580) for our experiments.

dataset	artifact	controlled?	number samples	number classes	biased class	p-bias (VGG-16 / ResNet-18 / Efficientnet-B0)	train / val / test split
Bone Age	brightness	yes	12,611	5	92-137 months	20% / 20% / 20%	80%/10%/10%
ISIC2019	LSB	yes	25,331	8	Melanoma	8.0%/12.5%/8.0%	80%/10%/10%
ImageNet	timestamp	yes	1,331,167	1000	“tench” (n01440764)	50% / 50% / 50%	86%/10%/ 4%
CelebA	collar	no	202,599	2	blonde hair	6% / 6% / 6%	80%/10%/10%

Table A.2: Training details for models considered in experiments, namely VGG-16, ResNet-18 and EfficientNet-B0.

model	optimizer	loss	learning rate	epochs
				(Bone Age / ISIC / ImageNet / CelebA)
VGG-16	SGD	Cross Entropy	0.005	100/150/13/40
ResNet-18	SGD	Cross Entropy	0.005	100/150/ 8/40
EfficientNet-B0	Adam	Cross Entropy	0.001	100/150/ 5/40

A.4 Concept Activation Vectors

For the computation of CAVs, we collect the activations of the last convolutional layer of each model. For a convolutional layer with m filters, activations are defined as $\mathbf{a}^{\text{conv}}(\mathbf{x}) \in \mathbb{R}^{m \times w \times h}$ with spatial dimension of width w and height h . Additionally, we perform max-pooling over the spatial dimension of each feature map to result in a single score per filter/neuron $\mathbf{a}(\mathbf{x}) \in \mathbb{R}^m$, given by

$$\mathbf{a}_i(\mathbf{x}) = \max_{v,q} \mathbf{a}_{i,v,q}^{\text{conv}}(\mathbf{x}). \quad (\text{A.1})$$

All CAVs are computed on the artifact samples and non-artifact samples of the biased class (ImageNet: “tench”, CelebA: “blonde”, Bone Age: “92-137 months”, ISIC: “Melanoma”) in the training set.

CAV Optimizer In the following, we will briefly describe ridge, lasso and SVM regression. The main aim of all methods, in our settings, is to linearly separate two clusters (described by concept label $t_i \in \{0, 1\}$) via a hyperplane, where vector \mathbf{h} describes the normal to the plane.

Lasso regression [35] is given by minimizing residuals $r_n = (t_n - \mathbf{a}(\mathbf{x}_n) \cdot \mathbf{h} - h_0)$ as

$$\mathbf{h}^{\text{lasso}} : \min_{\mathbf{h}, h_0} \left\{ \frac{1}{N} \sum_n r_n^2 + \lambda \sum_j |h_j| \right\} \quad (\text{A.2})$$

for all n samples \mathbf{x} , with additional bias term h_0 . Here, the term $\sum_j |h_j|$ leads to sparser coefficients, which also improves robustness against noise in the data.

Alternatively, ridge regression [16] is given by mini-

mizing

$$\mathbf{h}^{\text{ridge}} : \min_{\mathbf{h}, h_0} \left\{ \frac{1}{N} \sum_n r_n^2 + \lambda \sqrt{\sum_j h_j^2} \right\}, \quad (\text{A.3})$$

with an L_2 -norm term for the elements of \mathbf{h} .

Further, logistic regression performs maximum likelihood estimation for probabilities $p_n = \frac{1}{1 + e^{-\mathbf{a}(\mathbf{x}_n) \cdot \mathbf{h} - h_0}}$, leading to the minimization of

$$\mathbf{h}^{\text{logistic}} : \min_{\mathbf{h}, h_0} \left\{ - \sum_n t_n \ln(p_n) + (1 - t_n) \ln(1 - p_n) \right\}. \quad (\text{A.4})$$

Lastly, SVMs [9] try to find a hyperplane representing the largest separation (or margin) between the two class distributions. Therefore, a hinge-loss is defined as $l_n = \max(0, 1 - t_n^*(\mathbf{a}_n \cdot \mathbf{h} - h_0))$, leading to the minimization of

$$\mathbf{h}^{\text{SVM}} : \min_{\mathbf{h}, h_0} \left\{ \frac{1}{N} \sum_n l_n + \lambda \sqrt{\sum_j h_j^2} \right\} \quad (\text{A.5})$$

with additional L_2 regularization term, and labels $t_n^* = 2t_n - 1$.

B Detailed CAV Alignment Results

In the following, more details regarding the qualitative and quantitative experiments of Section 4.2 are given.

Quantitative Alignment

In the quantitative experiment, we measure the change in activation when the (known) bias is added to an input, and compute the cosine similarity between activation

Table A.3: Best performing hyperparameter values λ , as measured on the validation sets, for model correction methods RRR and RR-CIArC on the Bone Age, ISIC, ImageNet, and CelebA datasets for VGG-16, ResNet-18, and EfficientNet-B0 architectures.

		Bone Age	ISIC	ImageNet	CelebA
VGG-16	RRR	$5 \cdot 10^{-2}$	$5 \cdot 10^1$	10^2	$5 \cdot 10^5$
	RR-CIArC	10^8	$5 \cdot 10^8$	$5 \cdot 10^5$	$5 \cdot 10^8$
ResNet-18	RRR	10^2	$5 \cdot 10^2$	$5 \cdot 10^2$	$5 \cdot 10^5$
	RR-CIArC	$5 \cdot 10^9$	10^{11}	10^4	$5 \cdot 10^8$
EfficientNet-B0	RRR	$5 \cdot 10^1$	$5 \cdot 10^2$	1	$5 \cdot 10^6$
	RR-CIArC	$5 \cdot 10^{11}$	$5 \cdot 10^9$	$5 \cdot 10^5$	$5 \cdot 10^{11}$

change and CAV, as given by Equations (7) and (8) in the main paper. For the VGG-16 model, signal-CAV performed significantly better than the CAVs of regression-based optimizers. In Figure A.2, the results for ResNet-18 and EfficientNet-B0 architectures are shown as well, depicting a similar trend as for VGG-16, with signal-CAV performing best.

In general, the mean alignment \bar{s} (over *all* samples) is higher than the sample-wise alignment s (for *each* sample). For individual samples, the alignment can be small, when, *e.g.*, the bias transformation does not have a strong impact or is not visible, as shown in Figure A.3, where we show high and low alignment examples for the VGG-16 model.

Qualitative Alignment

In the qualitative alignment experiment, we compute CAV localization heatmaps (using LRP), that tend to localize the concept that a CAV describes. In Figures A.4 to A.15, we present further localization examples for the VGG-16 model. Signal-CAVs tend to localize the artifacts most precisely. For instance, looking at CelebA bias localizations in Figures A.4 - A.6, both, SVM- and ridge CAVs, include noisy background features, *e.g.*, for samples 3416 (*row 5, column 2*), 6948 (*row 8, column 10*), or 8190 (*row 9, column 12*). In contrast, signal CAVs precisely localize the artifact (here: *collar*) in input space.

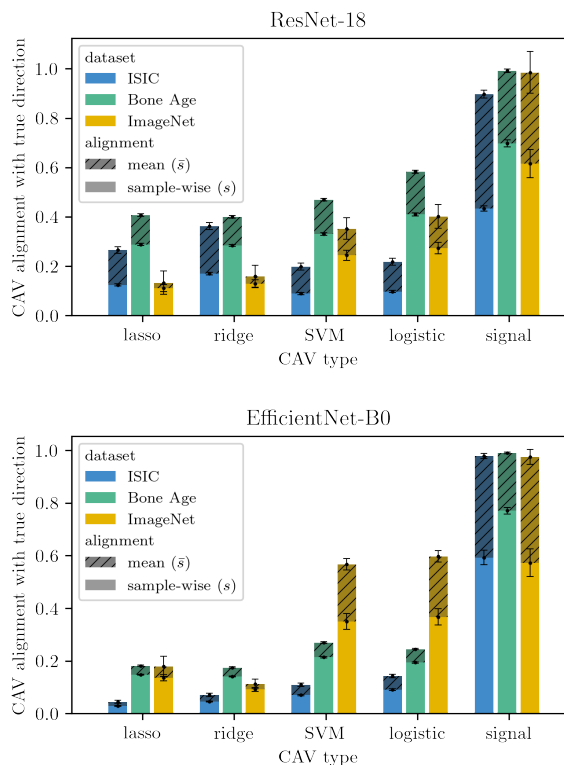


Figure A.2: Qualitative CAV alignment experiments for the ResNet-18 and EfficientNet-B0 architectures using different CAV optimizers.

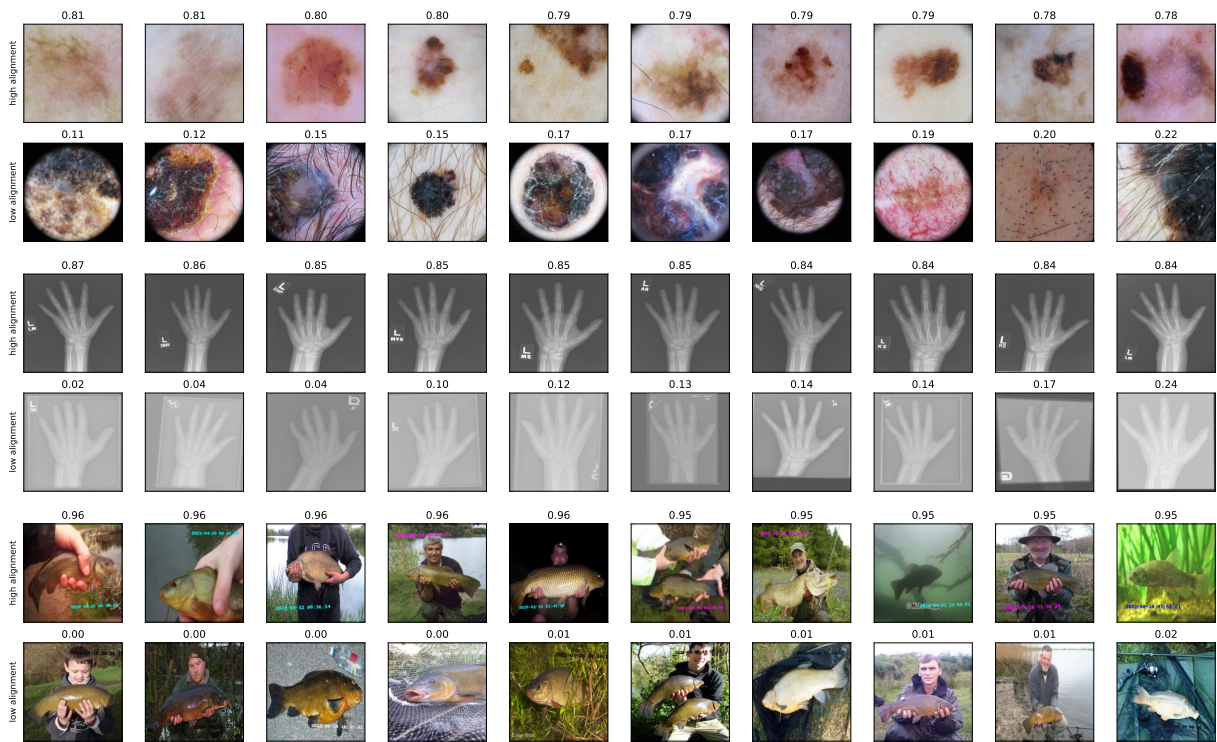


Figure A.3: Examples of biased samples, where the signal-CAV is high or low aligned with the change in activations, when the bias is added for the VGG-16 model. Alignment scores s are given above each input sample. (Top): ISIC, (Middle): Bone Age, (Bottom): ImageNet. Interestingly, low alignment scores s often occur when the artifact transformation barely affects the input sample, *e.g.*, when adding a black timestamp to a dark background (ImageNet), or when increasing the brightness for already above-average bright samples (Bone Age).



Figure A.4: Examples of signal-CAV localizations through LRP attributions for the CelebA bias (collar). Note, that signal-CAVs precisely localize most artifacts. In contrast, both ridge- and SVM-CAVs, include noisy background features in some cases, *e.g.*, for samples 3416 (row 5, column 2), 6948 (row 8, column 10), or 8190 (row 9, column 12), as seen in Figures A.5 and A.6.



Figure A.5: Examples of ridge-CAV localizations through LRP attributions for the CelebA bias (collar). Note, that a few localizations include noisy background features, *e.g.*, for samples 3416 (row 5, column 2), 6948 (row 8, column 10), or 8190 (row 9, column 12). In contrast, signal-CAVs precisely localize these artifacts (see Figure A.4)



Figure A.6: Examples of SVM-CAV localizations through LRP attributions for the CelebA bias (collar). Note, that a few localizations include noisy background features, *e.g.*, for samples 3416 (row 5, column 2), 6948 (row 8, column 10), or 8190 (row 9, column 12). In contrast, signal-CAV's precisely localize these artifacts (see Figure A.4)

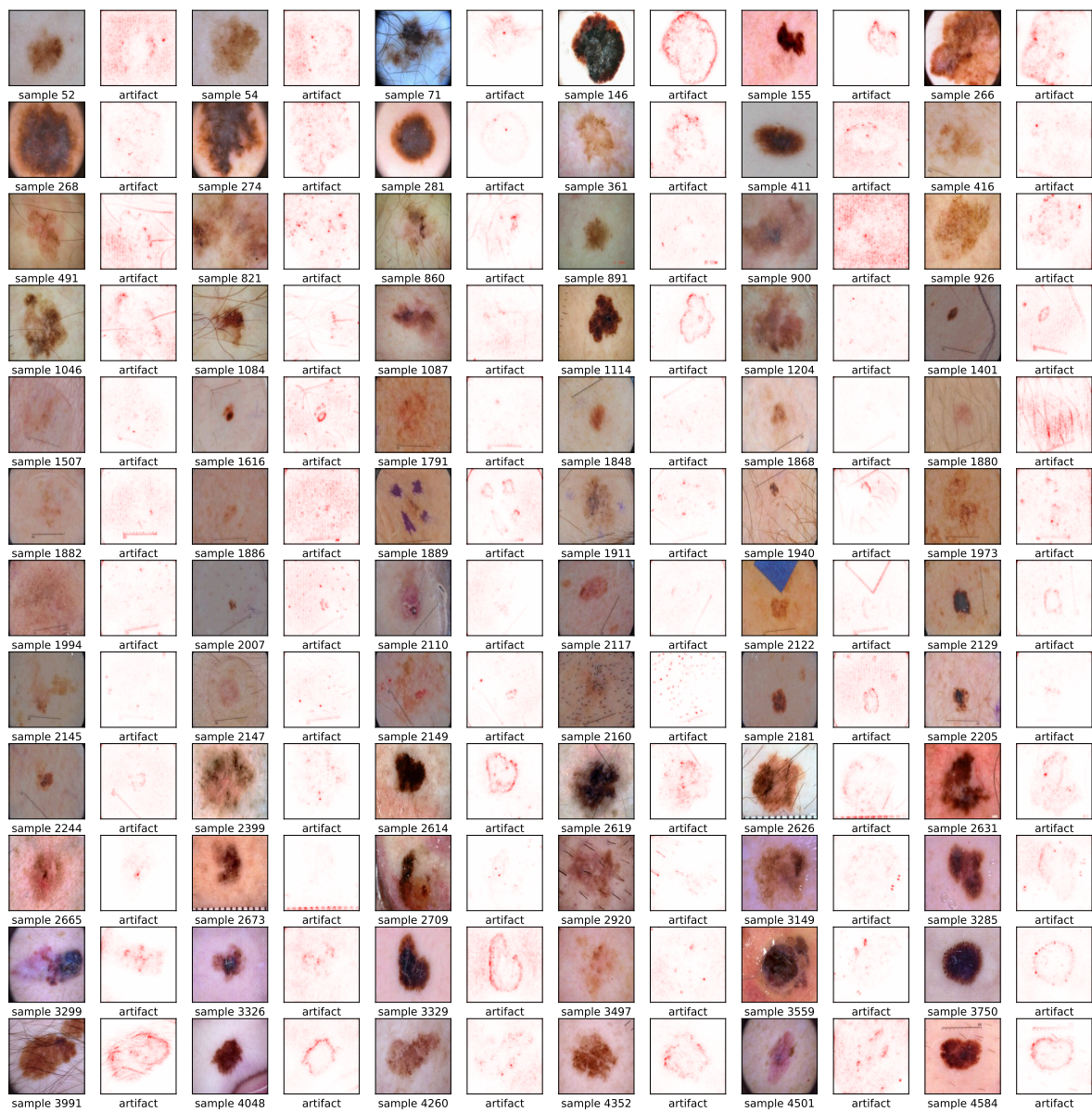


Figure A.7: Examples of signal-CAV localizations through LRP attributions for the ISIC bias (LSB attack). Best viewed digitally.

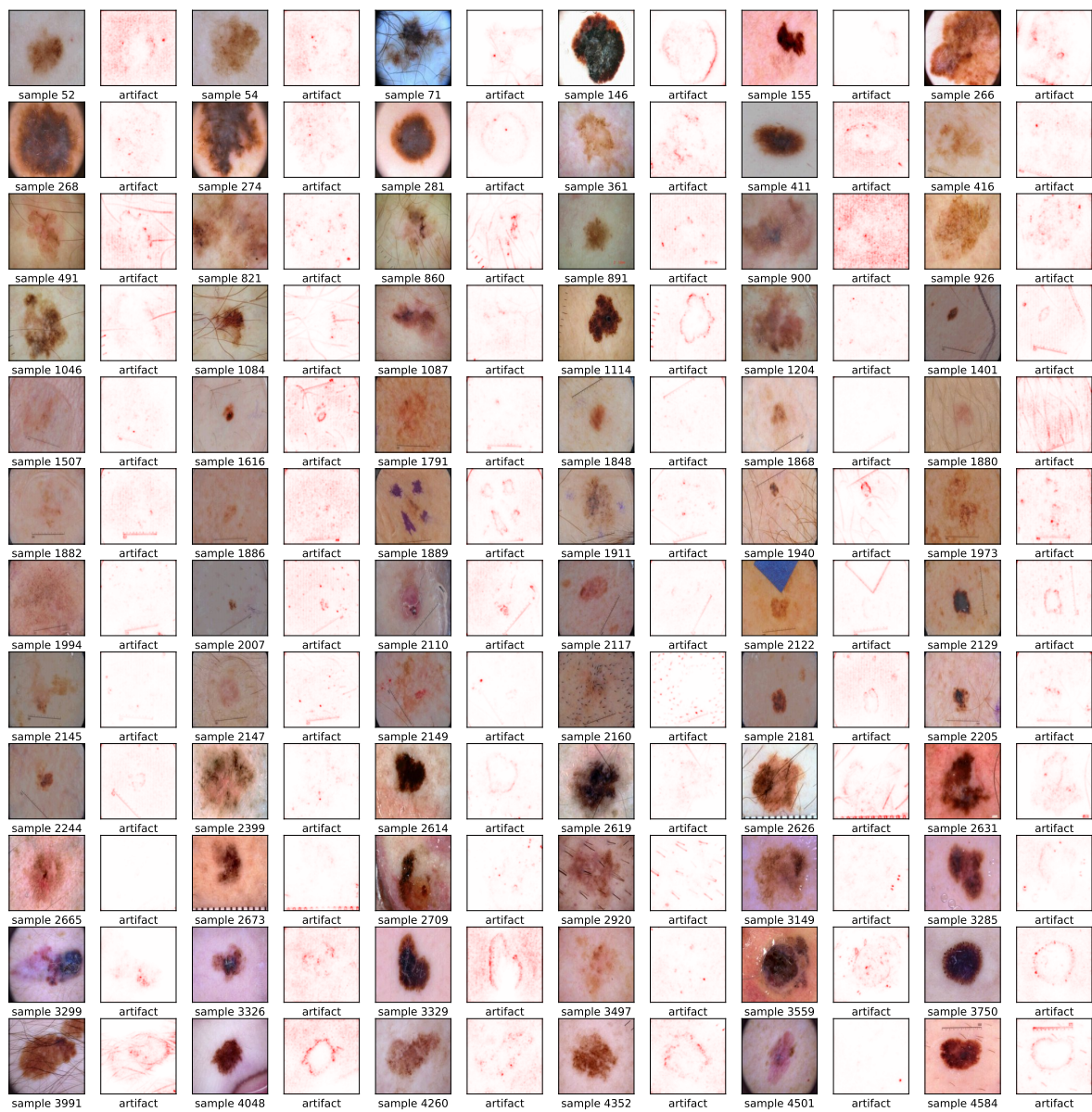


Figure A.8: Examples of ridge-CAV localizations through LRP attributions for the ISIC bias (LSB attack). Best viewed digitally.

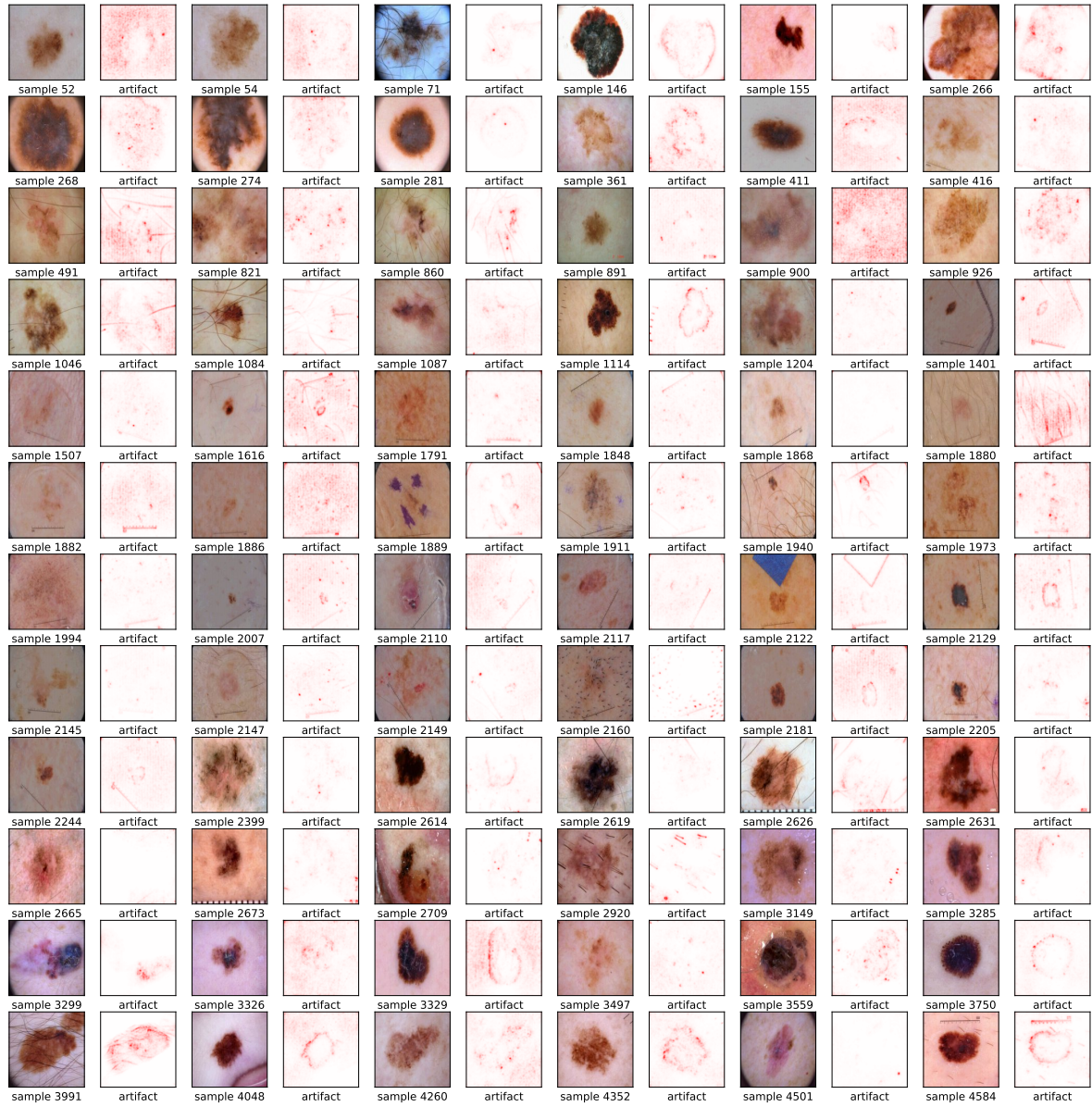


Figure A.9: Examples of SVM-CAV localizations through LRP attributions for the ISIC bias (LSB attack). Best viewed digitally.

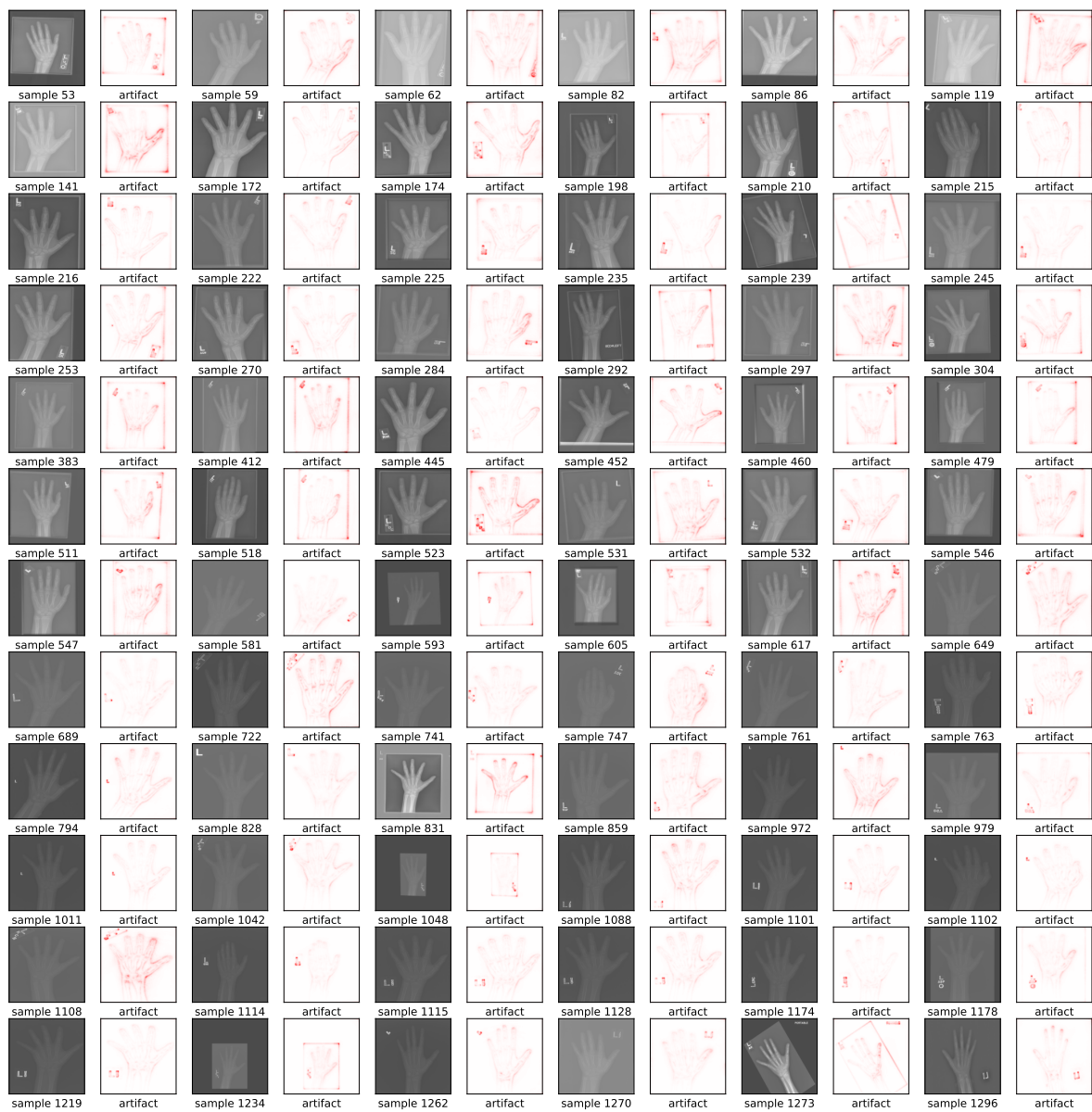


Figure A.10: Examples of signal-CAV localizations through LRP attributions for the Bone Age bias (brightness). Best viewed digitally.

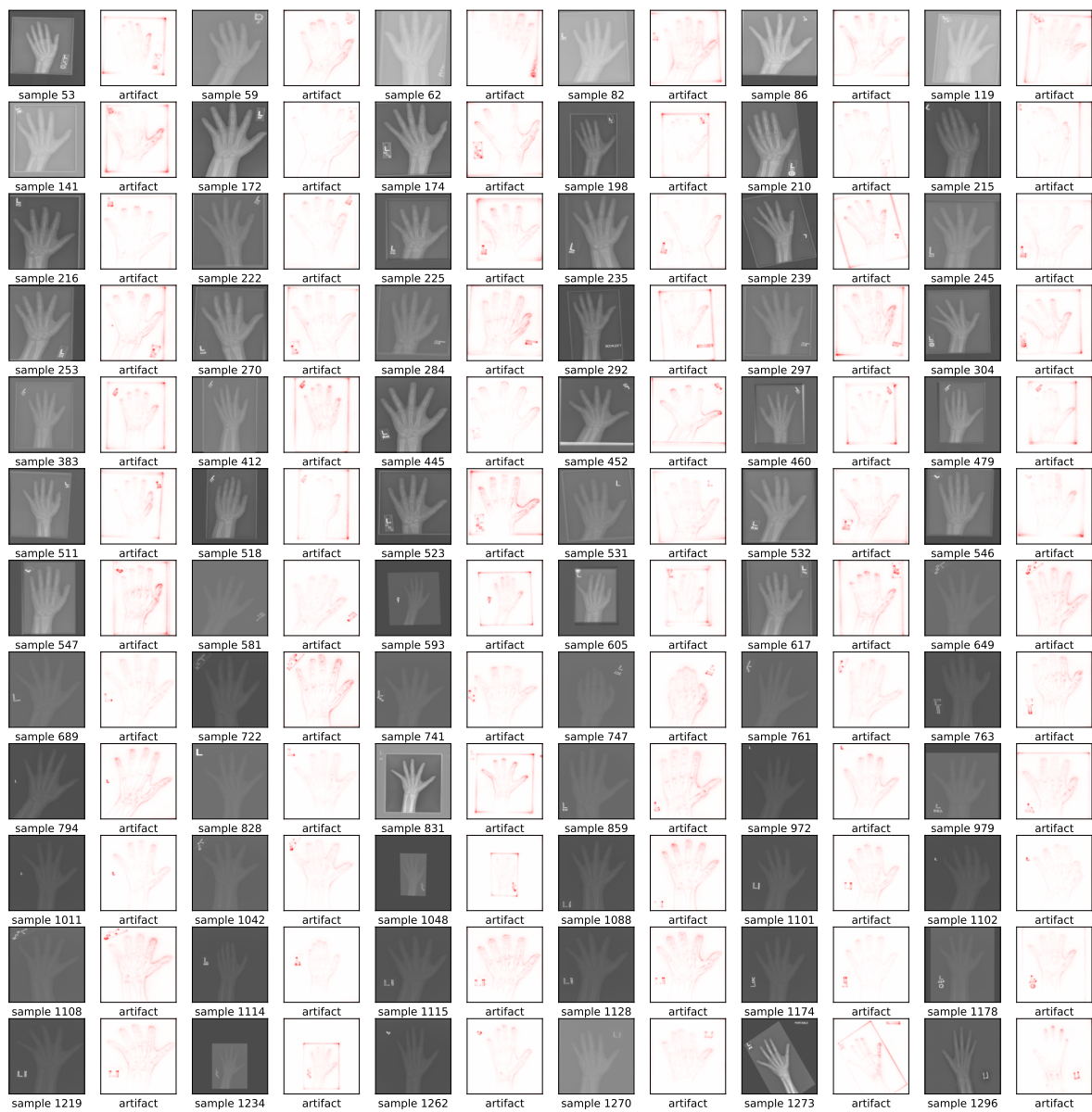


Figure A.11: Examples of ridge-CAV localizations through LRP attributions for the Bone Age bias (brightness). Best viewed digitally.

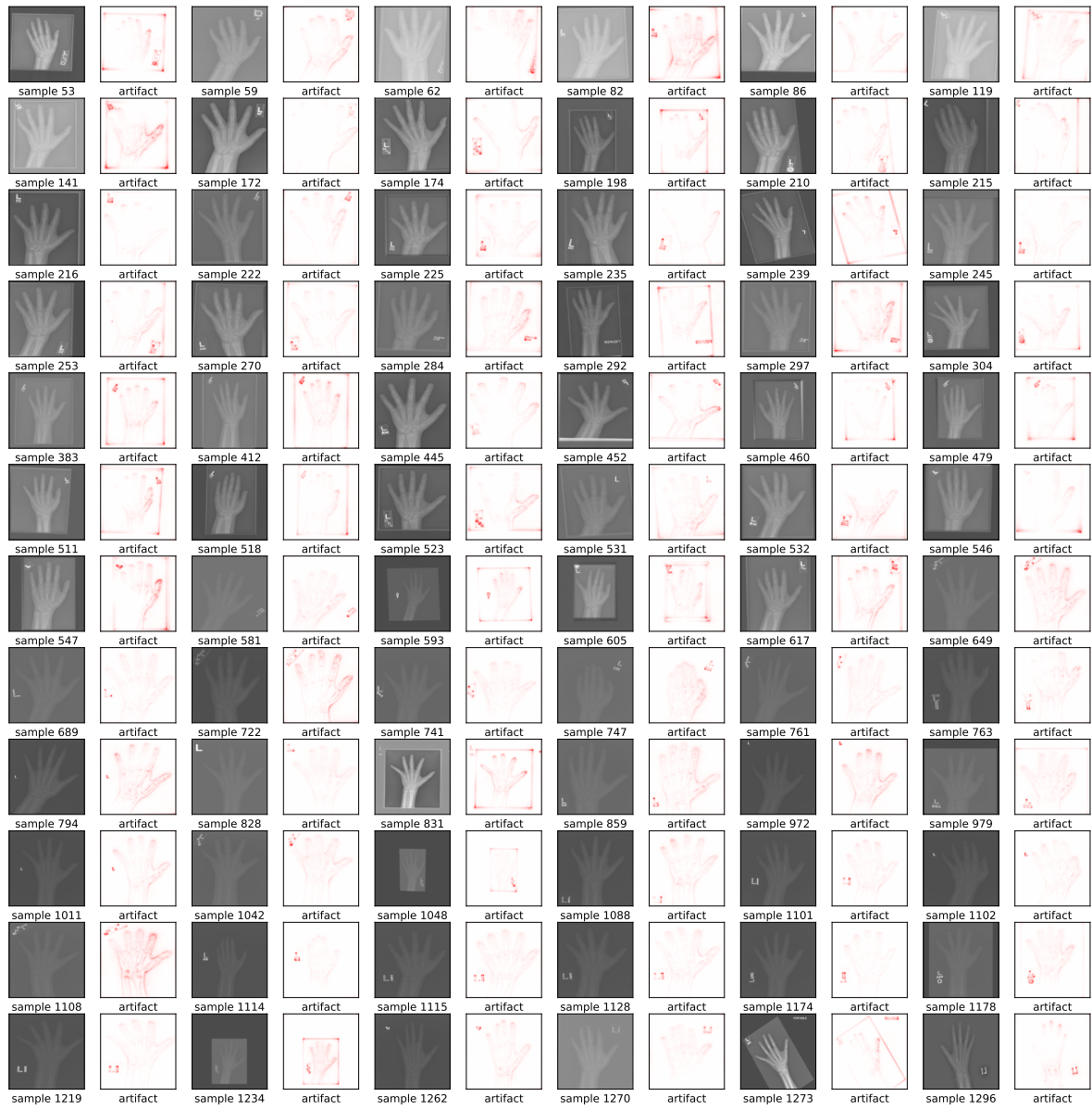


Figure A.12: Examples of SVM-CAV localizations through LRP attributions for the Bone Age bias (brightness). Best viewed digitally.



Figure A.13: Examples of signal-CAV localizations through LRP attributions for the ImageNet bias (timestamp). Best viewed digitally.



Figure A.14: Examples of ridge-CAV localizations through LRP attributions for the ImageNet bias (timestamp). Best viewed digitally.



Figure A.15: Examples of SVM-CAV localizations through LRP attributions for the ImageNet bias (timestamp). Best viewed digitally.

C Detailed Model Correction Results

In the following, we present more detailed results on the model correction experiment in Section 4.3.

In Tables A.4 and A.5, we extend the results presented in Table 1 in the main paper, presenting model correction results using the methods of RRR, CIArC methods A-CIArC, P-CIArC, and RR-CIArC, as well as *Vanilla*. We now include TCAV sensitivity (TCAV_{sens}), input-level bias relevance R_{bias} , and standard errors for all metrics. Here, TCAV sensitivity is given as

$$\text{TCAV}_{\text{sens}} = \frac{1}{|\mathcal{X}_{\text{bias}}|} \sum_{\mathbf{x} \in \mathcal{X}_{\text{bias}}} \left| \nabla_{\mathbf{a}} \tilde{f}(\mathbf{a}(\mathbf{x})) \cdot \mathbf{h} \right|, \quad (\text{A.6})$$

taking into account the magnitude of latent bias sensitivity, compared to the TCAV metric used in Equation (9), which only uses the sign.

The input relevances R_{bias} are computed via Layer-wise Relevance Propagation (LRP) [3] heatmaps, and input-level localizations of the biases. Please note, that only the biases in CelebA and ImageNet are localized, and thus reported. R_{bias} is given as the fraction of (absolute) relevance on the bias over the total (absolute relevance). Localizing the bias through mask \mathbf{M} with entries $\mathbf{M}_i \in \{0, 1\}$ for each input pixel i , we have

$$R_{\text{bias}} = \frac{\sum_i |\mathbf{R}_i \mathbf{M}_i|}{\sum_j |\mathbf{R}_j|} \in [0, 1]. \quad (\text{A.7})$$

As reported in Tables A.4 and A.5, in all experiments RR-CIArC results in the smallest bias sensitivities (TCAV_{sens}), except for ImageNet and the VGG-16, where RRR results in slightly smaller magnitudes. Regarding R_{bias} , RRR often results in the lowest scores, which can be expected due to the more direct regularization of RRR through input-gradients. Here, RR-CIArC however, significantly lowers R_{bias} compared to A- and P-CIArC.

Further, we provide the model correction results for all methods and all tested hyperparameters (RR-CIArC and RRR) in Figure A.16, showing the test accuracy on biased and clean test set in form of a scatter plot. Favorable is a high accuracy on both sets, *i.e.* a position of points in the top right corner. It can be seen, that RR-CIArC usually shows the best trade-off between low bias sensitivity (high accuracy on biased set) and accuracy (on clean set).

C.1 Runtime

To measure the runtimes in Section 4.3, we use an NVIDIA Tesla V100 graphics card with 32 GB memory (Tesla V100-PCIE-32GB) and an Intel Xeon Gold 6150 CPU with 2.7 GHz processor base frequency. Results for VGG-16, ResNet-18, and EfficientNet-B0 are

provided in Table A.6. For each dataset, model and correction method, we perform 10 runs and report the mean absolute and relative (to Vanilla training) time per epoch. Notably, on top of the requirement of input-level annotation masks for data artifacts, RRR results in much larger runtimes for the EfficientNet architecture, with an increase of up to 1300 % (750 % on average) compared to Vanilla training. We pinpoint the high increase in runtime to the parameter update step, where the gradient of the loss is computed. The computational graph appears to expand significantly, resulting in a considerably higher volume of computations required for parameter updates.

D Class-specific Model Correction

To choose *selected* classes for our experiments in Sec. 4.4 in the main paper, we measure which classes react most strongly, *i.e.*, show the largest absolute increase in logit value, for inserted timestamp artifacts. To achieve this, we construct two datasets: A *clean* dataset without artifacts and a *poisoned* dataset, with the artifact inserted into all samples from all classes. We then measure the difference in model outputs between *clean* and *poisoned* dataset for pre-trained VGG-16, ResNet-18 and EfficientNet-B0 models. The top-20 classes with the largest increase for each architecture are listed in Table A.7. In accordance with Figure 5 (main paper), we show the absolute accuracy difference between the Vanilla model and corrected models for *selected* and *random* classes for ResNet-18 and EfficientNet-B0 in Figure A.17. Similar trends as for VGG-16 can be observed: While class-inspecific approaches, *e.g.*, A-CIArC, lead to accuracy drops for selected classes, class-specific approaches, *i.e.*, RRR and RR-CIArC face no significant accuracy changes for both, random and selected classes. Interestingly, P-CIArC leads to an accuracy gain for selected classes for ResNet-18. This is due to the fact that, instead of removing the artifact direction, P-CIArC can also *add* the direction, if it is present to a below-average degree in a given sample. This can boost the classification performance of selected classes, relying on concepts related to the timestamp artifact.

Table A.4: Detailed model correction results including standard errors for Bone Age and ISIC experiments. We report model accuracy (in %) on *clean* and *biased* test sets, TCAV bias score, TCAV sensitivity ($\text{TCAV}_{\text{sens}}$), as well as R_{bias} . The latter is only shown for localized artifacts. Higher scores are better for accuracy, lower scores are better for $\text{TCAV}_{\text{sens}}$ and R_{bias} , and scores close to 50% are best for TCAV, with best scores bold.

model method	Bone Age					ISIC					
	<i>clean</i>	<i>biased</i>	TCAV (%)	$\text{TCAV}_{\text{sens}} (\times 10^3)$	R_{bias}	<i>clean</i>	<i>biased</i>	TCAV (%)	$\text{TCAV}_{\text{sens}} (\times 10^3)$	R_{bias}	
VGG-16	<i>Vanilla</i>	78.8 ± 1.2	49.8 ± 1.4	85.8 ± 0.1	5.58 ± 0.01	-	76.2 ± 0.8	34.9 ± 0.9	83.9 ± 0.1	3.68 ± 0.01	-
	RRR	78.8 ± 1.2	49.8 ± 1.4	85.7 ± 0.1	5.58 ± 0.01	-	76.7 ± 0.8	42.8 ± 1.0	71.7 ± 0.1	2.65 ± 0.01	-
	P-ClArC	78.9 ± 1.1	77.4 ± 1.2	66.0 ± 0.1	1.67 ± 0.01	-	75.1 ± 0.9	49.0 ± 1.0	76.7 ± 0.1	2.86 ± 0.01	-
	A-ClArC	77.8 ± 1.2	69.0 ± 1.3	65.7 ± 0.1	3.11 ± 0.01	-	75.2 ± 0.9	49.5 ± 1.0	64.8 ± 0.1	2.14 ± 0.01	-
	RR-ClArC	78.8 ± 1.2	77.7 ± 1.2	52.4 ± 0.1	0.44 ± 0.01	-	74.3 ± 0.9	57.0 ± 1.0	48.8 ± 0.1	0.12 ± 0.01	-
ResNet-18	<i>Vanilla</i>	75.1 ± 1.2	46.3 ± 1.4	100.0 ± 0.1	3.01 ± 0.01	-	81.8 ± 0.8	56.8 ± 1.0	100.0 ± 0.1	8.19 ± 0.01	-
	RRR	74.5 ± 1.2	47.9 ± 1.4	100.0 ± 0.1	2.78 ± 0.01	-	78.7 ± 0.8	61.1 ± 1.0	100.0 ± 0.1	6.59 ± 0.01	-
	P-ClArC	75.0 ± 1.2	70.7 ± 1.3	60.3 ± 0.2	1.20 ± 0.01	-	60.8 ± 1.0	59.9 ± 1.0	100.0 ± 0.1	8.75 ± 0.01	-
	A-ClArC	74.8 ± 1.2	57.4 ± 1.4	33.9 ± 0.2	0.37 ± 0.01	-	77.1 ± 0.8	65.0 ± 0.9	98.2 ± 0.1	1.83 ± 0.01	-
	RR-ClArC	71.1 ± 1.3	74.2 ± 1.2	39.2 ± 0.2	0.07 ± 0.01	-	78.5 ± 0.8	71.2 ± 0.9	75.7 ± 0.1	0.11 ± 0.01	-
Efficient Net-B0	<i>Vanilla</i>	78.2 ± 1.2	44.3 ± 1.4	89.8 ± 0.1	1.71 ± 0.01	-	84.2 ± 0.7	62.9 ± 1.0	99.6 ± 0.1	5.39 ± 0.01	-
	RRR	78.4 ± 1.2	49.6 ± 1.4	79.1 ± 0.2	1.07 ± 0.01	-	83.1 ± 0.7	68.7 ± 0.9	85.4 ± 0.1	2.34 ± 0.01	-
	P-ClArC	65.2 ± 1.3	35.1 ± 1.3	2.1 ± 0.1	2.20 ± 0.01	-	19.7 ± 0.8	29.6 ± 0.9	100.0 ± 0.1	13.79 ± 0.02	-
	A-ClArC	78.0 ± 1.2	54.2 ± 1.4	63.9 ± 0.2	1.00 ± 0.01	-	77.7 ± 0.8	72.8 ± 0.9	68.5 ± 0.1	1.09 ± 0.01	-
	RR-ClArC	77.6 ± 1.2	70.3 ± 1.3	53.3 ± 0.2	0.07 ± 0.01	-	78.7 ± 0.8	75.6 ± 0.9	54.4 ± 0.1	0.10 ± 0.01	-

Table A.5: Detailed model correction results including standard errors for ImageNet and CelebA experiments. We report model accuracy (in %) on *clean* and *biased* test sets, TCAV bias score, TCAV sensitivity ($\text{TCAV}_{\text{sens}}$), as well as R_{bias} . Higher scores are better for accuracy, lower scores are better for $\text{TCAV}_{\text{sens}}$ and R_{bias} , and scores close to 50% are best for TCAV, with best scores bold.

model method	ImageNet					CelebA					
	<i>clean</i>	<i>biased</i>	TCAV (%)	$\text{TCAV}_{\text{sens}} (\times 10^3)$	R_{bias}	<i>clean</i>	<i>biased</i>	TCAV (%)	$\text{TCAV}_{\text{sens}} (\times 10^3)$	R_{bias}	
VGG-16	<i>Vanilla</i>	68.7 ± 0.7	43.5 ± 0.7	62.9 ± 0.1	1.07 ± 0.01	19.6 ± 1.9	93.7 ± 2.6	82.8 ± 2.2	36.8 ± 0.2	0.92 ± 0.01	13.6 ± 1.3
	RRR	68.6 ± 0.7	49.6 ± 0.7	54.6 ± 0.1	0.62 ± 0.01	6.8 ± 0.8	93.7 ± 2.0	91.2 ± 1.7	42.6 ± 0.2	0.88 ± 0.01	2.0 ± 0.4
	P-ClArC	68.3 ± 0.7	62.6 ± 0.7	37.1 ± 0.1	0.30 ± 0.01	15.9 ± 1.3	56.6 ± 1.8	60.8 ± 3.3	19.3 ± 0.2	1.24 ± 0.01	4.3 ± 0.6
	A-ClArC	67.7 ± 0.7	60.9 ± 0.7	49.0 ± 0.1	0.47 ± 0.01	12.2 ± 1.1	93.0 ± 2.1	90.4 ± 1.7	44.2 ± 0.2	0.95 ± 0.01	9.5 ± 1.0
	RR-ClArC	68.5 ± 0.7	62.6 ± 0.7	49.1 ± 0.1	0.33 ± 0.01	8.7 ± 0.6	93.6 ± 1.9	92.6 ± 1.6	54.1 ± 0.2	0.09 ± 0.01	2.3 ± 0.4
ResNet-18	<i>Vanilla</i>	66.7 ± 0.7	52.9 ± 0.7	100.0 ± 0.1	4.35 ± 0.01	13.4 ± 0.9	96.8 ± 2.0	58.3 ± 3.2	21.4 ± 0.4	1.92 ± 0.01	19.2 ± 1.9
	RRR	66.4 ± 0.7	59.1 ± 0.7	7.7 ± 0.1	2.07 ± 0.01	7.1 ± 0.6	95.5 ± 2.8	74.7 ± 2.8	91.6 ± 0.3	1.86 ± 0.01	7.7 ± 1.1
	P-ClArC	67.0 ± 0.7	61.7 ± 0.7	80.5 ± 0.1	1.93 ± 0.01	13.5 ± 0.9	96.5 ± 2.4	64.4 ± 3.1	5.7 ± 0.2	2.03 ± 0.01	7.7 ± 1.0
	A-ClArC	65.0 ± 0.7	63.3 ± 0.7	87.8 ± 0.1	0.87 ± 0.01	11.3 ± 0.8	96.1 ± 2.4	62.9 ± 3.1	37.8 ± 0.5	1.43 ± 0.01	17.0 ± 1.8
	RR-ClArC	66.5 ± 0.7	64.0 ± 0.7	55.4 ± 0.1	0.54 ± 0.01	10.1 ± 0.7	95.8 ± 2.7	75.3 ± 2.8	60.5 ± 0.5	0.04 ± 0.01	9.1 ± 1.1
Efficient Net-B0	<i>Vanilla</i>	73.9 ± 0.6	53.2 ± 0.7	99.2 ± 0.1	3.02 ± 0.01	18.6 ± 1.6	96.6 ± 2.0	58.3 ± 3.2	24.8 ± 0.4	1.47 ± 0.02	26.1 ± 2.8
	RRR	73.9 ± 0.6	59.1 ± 0.7	65.9 ± 0.1	0.97 ± 0.01	13.2 ± 1.4	95.4 ± 2.7	75.6 ± 2.8	50.4 ± 0.5	1.09 ± 0.02	14.3 ± 1.8
	P-ClArC	74.1 ± 0.6	54.6 ± 0.7	20.8 ± 0.1	1.29 ± 0.01	20.5 ± 1.5	96.8 ± 1.6	55.0 ± 3.3	4.9 ± 0.2	0.85 ± 0.02	25.9 ± 2.5
	A-ClArC	71.4 ± 0.6	69.9 ± 0.6	90.5 ± 0.1	1.39 ± 0.01	18.9 ± 1.9	96.7 ± 2.2	60.6 ± 3.2	23.8 ± 0.4	1.27 ± 0.02	21.8 ± 2.6
	RR-ClArC	73.9 ± 0.6	70.8 ± 0.6	56.4 ± 0.1	0.95 ± 0.01	13.2 ± 1.4	92.0 ± 2.8	77.6 ± 2.7	42.6 ± 0.5	0.00 ± 0.01	21.3 ± 2.5

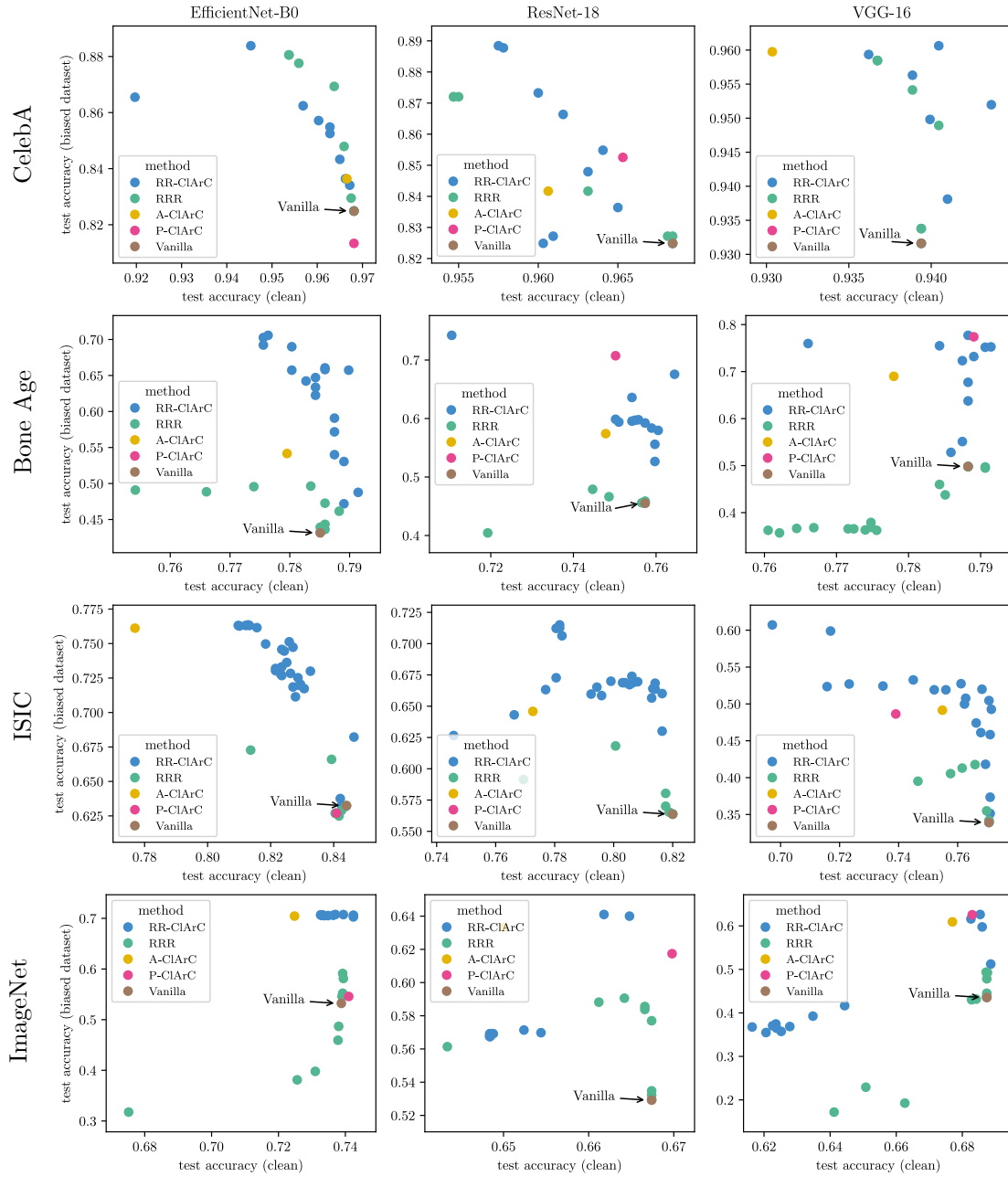


Figure A.16: More detailed model correction results in terms of accuracy on clean and biased test set, showing runs with all hyperparameters for RR-CIArC and RRR. Ideal is a position in the top right corner, *i.e.* a high accuracy on both sets.

Table A.6: Training times of all correction methods in seconds per epoch (*absolute*) and relative to Vanilla training (*relative*).

model	method	ImageNet		Bone		ISIC		CelebA	
		<i>absolute</i> (s)	<i>relative</i> (%)						
VGG-16	Vanilla	277.5 ± 3.6	100.0 ± 1.3	91.4 ± 0.1	100.0 ± 0.1	110.0 ± 0.2	100.0 ± 0.2	39.8 ± 0.1	100.0 ± 0.3
	RRR	412.8 ± 3.7	148.7 ± 1.4	147.8 ± 0.4	161.6 ± 0.4	218.7 ± 0.2	198.8 ± 0.2	73.2 ± 0.1	184.0 ± 0.2
	RR-CIArC	304.8 ± 8.4	109.8 ± 3.0	93.7 ± 0.3	102.4 ± 0.3	113.4 ± 0.2	103.1 ± 0.2	66.3 ± 0.1	166.7 ± 0.4
	P-CIArC	284.7 ± 8.1	102.6 ± 2.9	92.1 ± 0.5	100.7 ± 0.6	109.7 ± 0.3	99.7 ± 0.2	39.6 ± 0.1	99.5 ± 0.3
	A-CIArC	296.2 ± 11.9	106.7 ± 4.3	92.2 ± 0.6	100.9 ± 0.6	110.0 ± 0.1	100.0 ± 0.1	40.4 ± 0.3	101.7 ± 0.7
ResNet-18	Vanilla	262.1 ± 3.3	100.0 ± 1.3	88.4 ± 0.3	100.0 ± 0.4	105.6 ± 0.1	100.0 ± 0.1	27.2 ± 0.2	100.0 ± 0.6
	RRR	327.9 ± 11.8	125.1 ± 4.5	94.0 ± 0.3	106.4 ± 0.4	114.9 ± 0.3	108.8 ± 0.2	42.1 ± 0.1	154.4 ± 0.4
	RR-CIArC	267.8 ± 4.8	102.2 ± 1.8	88.6 ± 0.2	100.2 ± 0.2	106.6 ± 0.2	100.9 ± 0.2	35.2 ± 0.1	129.2 ± 0.4
	P-CIArC	259.0 ± 2.6	98.8 ± 1.0	88.0 ± 0.2	99.6 ± 0.2	105.7 ± 0.1	100.1 ± 0.1	27.1 ± 0.2	99.5 ± 0.7
	A-CIArC	255.1 ± 1.7	97.4 ± 0.6	88.0 ± 0.2	99.5 ± 0.2	105.6 ± 0.2	99.9 ± 0.2	27.8 ± 0.2	101.9 ± 0.8
Efficient Net-B0	Vanilla	265.9 ± 6.8	100.0 ± 2.5	88.0 ± 0.2	100.0 ± 0.2	105.1 ± 0.2	100.0 ± 0.2	30.4 ± 0.1	100.0 ± 0.5
	RRR	1476.5 ± 8.5	555.3 ± 3.2	998.3 ± 2.5	1134.7 ± 2.8	1382.7 ± 1.3	1315.6 ± 1.3	126.8 ± 0.3	417.8 ± 1.1
	RR-CIArC	277.2 ± 8.0	104.3 ± 3.0	89.0 ± 0.2	101.2 ± 0.2	107.7 ± 0.3	102.5 ± 0.2	46.7 ± 0.2	153.8 ± 0.7
	P-CIArC	270.0 ± 9.2	101.5 ± 3.5	88.3 ± 0.2	100.3 ± 0.3	105.3 ± 0.2	100.2 ± 0.2	30.2 ± 0.2	99.4 ± 0.6
	A-CIArC	266.4 ± 8.7	100.2 ± 3.3	88.5 ± 0.1	100.6 ± 0.1	105.7 ± 0.2	100.5 ± 0.2	30.7 ± 0.3	101.1 ± 1.1

Table A.7: *Selected* ImageNet classes that strongly react to the artificial timestamp artifact for VGG-16, ResNet-18, and EfficientNet-B0.

model	selected classes
VGG-16	“web site” (n06359193), “book jacket” (n07248320), “comic book” (n06596364), “oscilloscope” (n03857828), “scoreboard” (n04149813), “packet” (n03871628), “envelope” (n03291819), “modem” (n03777754), “menu” (n07565083), “cash machine” (n02977058), “bathing cap” (n02807133), “monitor” (n03782006), “nematode” (n01930112), “hand-held computer” (n03485407), “cassette” (n02978881), “vending machine” (n04525305), “balance beam” (n02777292), “digital clock” (n03196217), “racket” (n04039381), “brassiere” (n02892767)
	“web site” (n06359193), “envelope” (n03291819), “comic book” (n06596364), “oscilloscope” (n03857828), “packet” (n03871628), “menu” (n07565083), “book jacket” (n07248320), “scoreboard” (n04149813), “beaker” (n02815834), “balance beam” (n02777292), “stage” (n04296562), “monitor” (n03782006), “rule” (n04118776), “odometer” (n03841143), “carton” (n02971356), “bathing cap” (n02807133), “jigsaw puzzle” (n03598930), “panpipe” (n03884397), “bikini” (n02837789), “screen” (n04152593)
ResNet-18	“web site” (n06359193), “book jacket” (n07248320), “menu” (n07565083), “comic book” (n06596364), “monitor” (n03782006), “carton” (n02971356), “street sign” (n06794110), “crane” (n03126707), “panpipe” (n03884397), “envelope” (n03291819), “digital clock” (n03196217), “magnetic compass” (n03706229), “jigsaw puzzle” (n03598930), “packet” (n03871628), “odometer” (n03841143), “vending machine” (n04525305), “screen” (n04152593), “groenendael” (n02105056), “scoreboard” (n04149813), “gown” (n03450230)
EfficientNet-B0	“web site” (n06359193), “book jacket” (n07248320), “menu” (n07565083), “comic book” (n06596364), “monitor” (n03782006), “carton” (n02971356), “street sign” (n06794110), “crane” (n03126707), “panpipe” (n03884397), “envelope” (n03291819), “digital clock” (n03196217), “magnetic compass” (n03706229), “jigsaw puzzle” (n03598930), “packet” (n03871628), “odometer” (n03841143), “vending machine” (n04525305), “screen” (n04152593), “groenendael” (n02105056), “scoreboard” (n04149813), “gown” (n03450230)

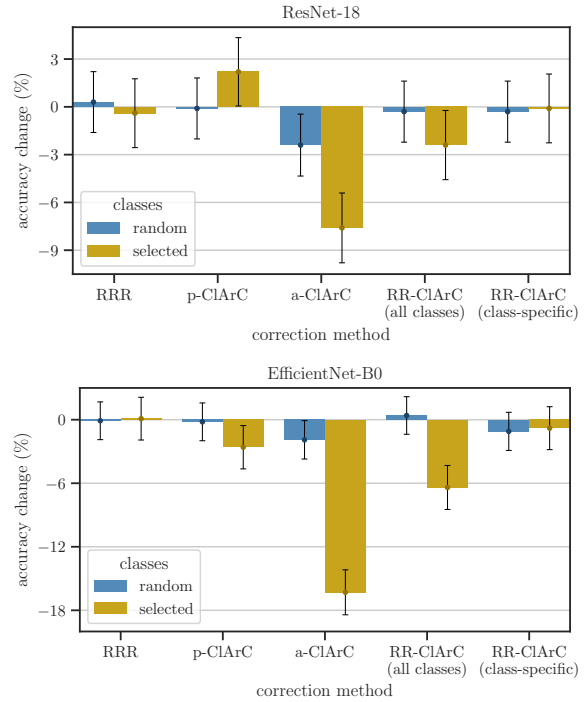


Figure A.17: Impact of model correction for the timestamp bias (ImageNet) on model accuracy for random and selected classes for ResNet-18 (*top*) and EfficientNet-B0 (*bottom*). While A-CIArC is class-inspecific and leads to a drop in accuracy for selected classes, RRR and RR-CIArC *only* unlearn the artifact for a specific class. Interestingly, while leading to an accuracy drop for selected classes for EfficientNet-B0, P-CIArC causes an accuracy gain for ResNet-18. This can happen when P-CIArC adds the bias-CAV direction instead of removing it for certain samples containing below-average artifact direction. For selected classes, *i.e.*, classes that leverage related concepts, this can lead to performance gains.

E Ablation Study

In the following, we provide more details and experiments for the ablation study in Section 4.5 of the main paper.

Regularization Strength

The effect of using different regularization strengths λ is shown in Figure A.18 for the VGG-16 model, where the accuracy on the biased test set is shown for various regularization strengths. Further, we show LRP explanation heatmaps for a subset of the λ values. In the figure, it is apparent, that the higher the regularization strength, the higher the accuracy up to a turning point, where regularization becomes too strong, and the accuracy falls again. Regarding the heatmaps, it can be seen, that the relevance of the bias decreases most, when close to the turning point, followed by insensible heatmaps (Bone Age, ISIC) for higher regularization.

Gradient Target & Loss Aggregation

RR-ClArC as in Equation (5) uses the gradient w.r.t. the output logits and squares the dot product between gradient and CAV. In principle, also other gradient targets (*e.g.* sum of log-probability scores as in RRR) and aggregation schemes (L_1 -norm, cosine similarity) can be used.

Specifically, the work of RRR *i.e.* $\nabla_{\mathbf{x}} \sum_k \log(p_k)$ with softmax probability $p_k = \frac{e^{f_k(\mathbf{x})}}{\sum_l e^{f_l(\mathbf{x})}}$. However, it is to note, that using the sum of log-probabilities does not allow the flexibility for class-specific corrections as given with logits in Equation (5) through annotation vector \mathbf{m} . For the ablation study, we compare gradients w.r.t. logits given by $(\mathbf{m})_i = 1$, regularizing all classes uniformly, and $(\mathbf{m})_i \in_R \{-1, 1\}$, assigning a random sign to each class.

The motivation behind choosing $(\mathbf{m})_i \in_R \{-1, 1\}$ is, that when accumulating the gradient from multiple logits at once (in one backward pass), the bias concept might positively contribute to one class, and negatively to another, leading to a smaller gradient, as the contributions cancel one another. Summing over the logits with a random sign, *i.e.* choosing $(\mathbf{m})_i \in_R \{-1, 1\}$ as used in Eq. (5), further improves performance by mitigating the cancelation effect.

The final accuracy on biased and clean test set of the VGG-16 model is shown in Figure A.19 for L_1 , L_2 and cosine similarity as the loss aggregation scheme. It is apparent, that using the gradient w.r.t. to the logits is more stable compared to log-probabilities. Whereas log-probabilities seem to result in a favorable regularization for Bone Age (strongly increasing clean test accuracy), they fail in effectively unlearning the bias for ImageNet. Overall, choosing $(\mathbf{m})_i \in_R \{-1, 1\}$ slightly improves

regularization compared to $(\mathbf{m})_i = 1$. Regarding the aggregation scheme, no approach shows significantly better results.

Fine-tuning Epochs

Another hyperparameter of RR-ClArC is the number of epochs for fine-tuning and unlearning of a bias concept. In Figure A.20, we show the convergence of the VGG-16 model for different regularization strengths in terms of accuracy on the clean and biased test set.

It can be seen, that lower regularizations tend to require more fine-tuning steps to converge, whereas higher learning rates are already converged after one epoch. Very high regularization strengths lead to a strong decrease in accuracy the more epochs are trained.

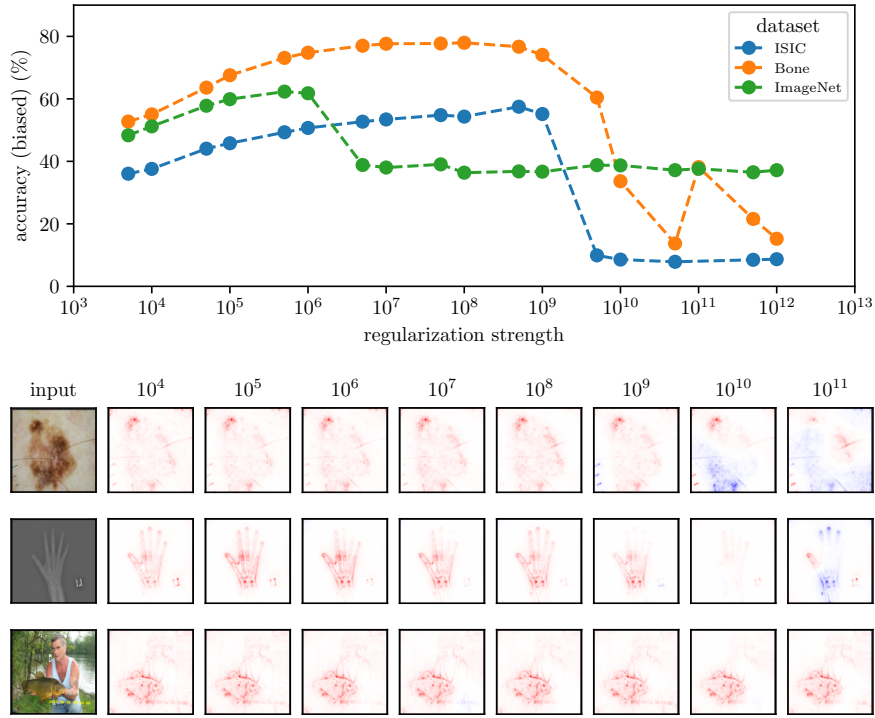


Figure A.18: The effect of different regularization strengths on accuracy of the biased test set and LRP heatmaps. Best viewed digitally.

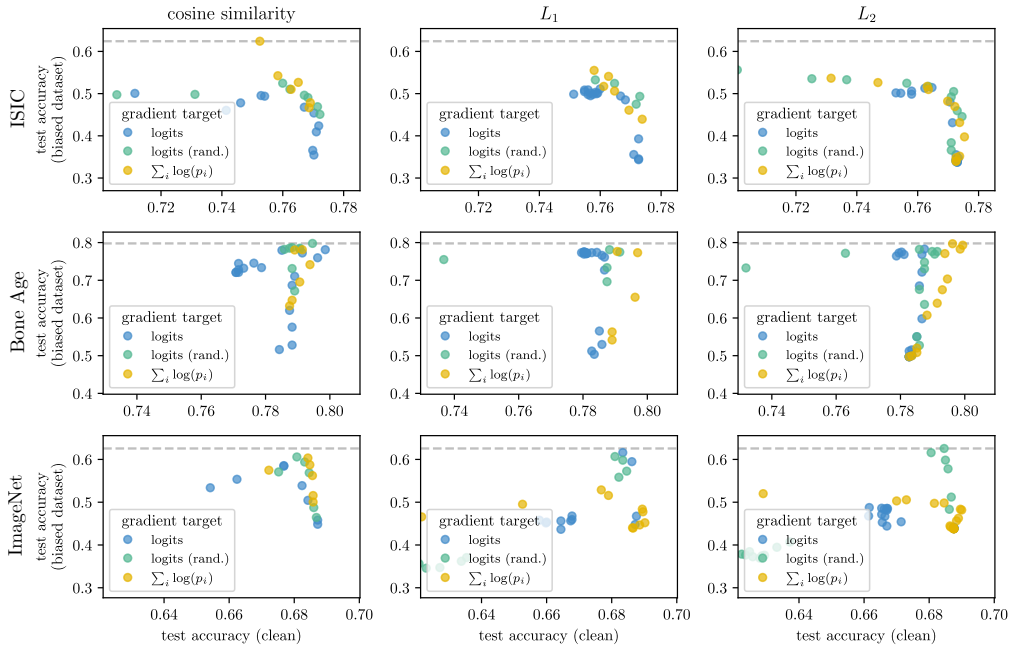


Figure A.19: The effect of different gradient targets and aggregation schemes for RR-CIArC with different regularization strengths for a VGG-16 model. Shown is the model accuracy on clean and biased test set.

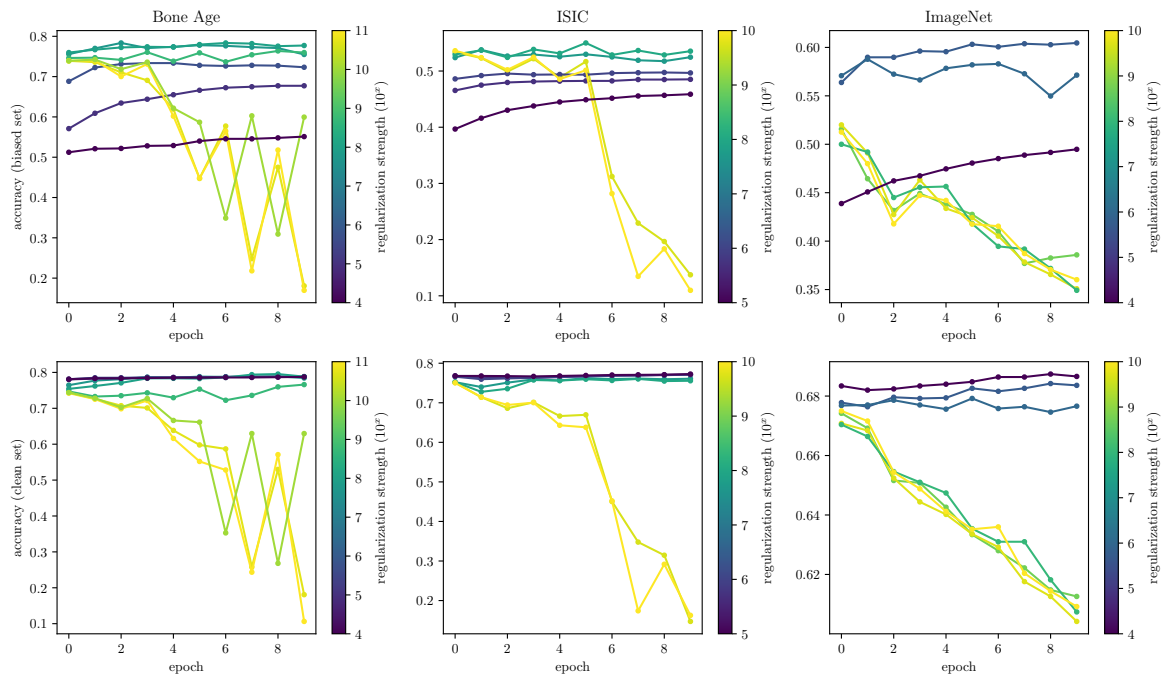


Figure A.20: The effect of the number of fine-tuning epochs on clean and biased test set accuracy. (*1st row*): Biased test set accuracy over epochs. (*2nd row*): Clean test set accuracy over epochs.